Cerebral Cortex, November 2015;25: 4450–4468

doi: 10.1093/cercor/bhv053
Advance Access Publication Date: 1 April 2015
Original Article

ORIGINAL ARTICLE

Beyond Columnar Organization: Cell Type- and Target Layer-Specific Principles of Horizontal Axon Projection Patterns in Rat Vibrissal Cortex

Rajeevan T. Narayanan[1], Robert Egger[1,2], Andrew S. Johnson[3], Huibert D. Mansvelder[4], Bert Sakmann[3], Christiaan P.J. de Kock[4,†], and Marcel Oberlaender[1,3,5,†]

[1]Computational Neuroanatomy Group, Max Planck Institute for Biological Cybernetics, Tuebingen, Germany, [2]Graduate School of Neural Information Processing, University of Tuebingen, Tuebingen, Germany, [3]Digital Neuroanatomy, Max Planck Florida Institute for Neuroscience, Jupiter , FL 33458, USA, [4]Center for Neurogenomics and Cognitive Research, Neuroscience Campus Amsterdam, VU University Amsterdam, The Netherlands, and [5]Bernstein Center for Computational Neuroscience, Tuebingen, Germany

Address correspondence to Computational Neuroanatomy Group, Max Planck Institute for Biological Cybernetics, Spemannstraße 38–44, Tuebingen 72076 Germany. Email: marcel.oberlaender@tuebingen.mpg.de (M. Oberlaender); Center for Neurogenomics and Cognitive Research, Neuroscience Campus Amsterdam, VU University Amsterdam, De Boelelaan 1087, 1081 HV Amsterdam, The Netherlands. Email: ckock@falw.vu.nl (C.P.J.de. Kock)

[†]Christiaan P.J. de Kock and Marcel Oberlaender share senior authorship.

Abstract

Vertical thalamocortical afferents give rise to the elementary functional units of sensory cortex, *cortical columns*. Principles that underlie communication between columns remain however unknown. Here we unravel these by reconstructing in vivo-labeled neurons from all excitatory cell types in the vibrissal part of rat primary somatosensory cortex (vS1). Integrating the morphologies into an exact 3D model of vS1 revealed that the majority of intracortical (IC) axons project far beyond the borders of the principal column. We defined the corresponding innervation volume as the *IC-unit*. Deconstructing this structural cortical unit into its cell type-specific components, we found asymmetric projections that innervate columns of either the same whisker row or arc, and which subdivide vS1 into 2 orthogonal [supra-]granular and infragranular strata. We show that such organization could be most effective for encoding multi whisker inputs. Communication between columns is thus organized by multiple highly specific horizontal projection patterns, rendering IC-units as the primary structural entities for processing complex sensory stimuli.

Key words: barrel cortex, excitatory, intracortical unit, multiwhisker, transcolumnar

Introduction

Long-range horizontal pathways have been recognized as an important and characteristic feature of the cortical circuitry for decades (Braitenberg 1962). However, methodological limitations and the long-standing dominance of the columnar concept (Mountcastle 1957), which emphasizes vertical connections,

have so far prevented from quantitative assesments of the organizational principles that underly horizontally projecting axons. Already in the 1950s, axonal degeneration induced by small lesions revealed the widespread horizontal extent of intracortical (IC) axonal connections (Nauta and Gygax 1954). Degeneration reached radii of up to 3.5 mm from the lesion site in the primary visual cortex (V1) of macaque monkeys (Fisken et al. 1975) and cats (Creutzfeldt et al. 1977). But it was not before the pioneering work of Gilbert and Wiesel (1979) that these extensive horizontal axons could be visualized. Surprisingly, the discovered axons traveled lateral distances of multiple millimeters without entry into the white matter. Such pathways were termed long-range "*intrinsic*" horizontal pathways (i.e., extrinsic: via the white matter). It became hence evident that the elementary functional unit of cortex, the cortical column, is connected both vertically across cytoarchitectonic layers and horizontally to neighboring columns.

Moreover, the patterns of transcolumnar pathways were shown to deviate between cortical areas. For example, horizontal projections within tree shrew (Rockland and Lund 1982; Rockland et al. 1982) and cat V1 (Gilbert and Wiesel 1983) form axon patches that interconnect columns of similar orientation tuning (Hubel and Wiesel 1959; Bosking et al. 1997). Similarly, in monkey prefrontal cortex (PFC) labeled axon terminals form a series of regularly spaced elongated stripes (Levitt et al. 1993). By analogy to the links between orientation columns in V1, these long-distance horizontal PFC pathways have been proposed to link clusters of neurons sharing similar memory fields (Goldman-Rakic 1995) or object selectivities (Rainer et al. 1998). In contrast, bulk injections of anterograde tracers into a barrel column (Woolsey and Van der Loos 1970) of the vibrissal part of rodent primary somatosensory cortex (vS1) revealed horizontal projections that give rise to an hourglass-shaped volume that asymmetrically interconnects columns representing facial whiskers of the same row along the snout (Bernardo et al. 1990). Asymmetries in the distribution of intrinsic, horizontal pathways were also reported in other cortical areas, such as the motor cortex (M1) of the monkey (Huntley and Jones 1991), cat (Keller 1993; Keller and Asanuma 1993), and rat (Weiss and Keller 1994), where horizontal axons project primarily in an anteroposterior orientation, linking regions related to the activation of related muscle groups.

Detailed understanding of the organizational principles that underlie area-specific intrinsic horizontal projection patterns will thus be key for unraveling common and/or specific mechanisms of cortical stimulus representation and multistimuli integration. However, despite earlier attempts to unravel these principles, answers to the question—*How are transcolumnar pathways organized at cellular levels?*—are still lacking. This gap in present concepts of cortical circuit organization arises primarily from 3 methodological limitations. First, most studies that investigated IC axons and synaptic innervation at cellular resolution were, so far, made in acute brain slices in vitro (Feldmeyer et al. 1999; Nikolenko et al. 2007; Lefort et al. 2009; Petreanu et al. 2009). There, substantial cutting of dendrites and axons conceals transcolumnar axon projections, resulting in circuit diagrams that are dominated by vertically organized translaminar pathways. Second, a more promising approach to uncover IC axonal organization is labeling individual neurons in vivo (Pinault 1996), which allows for reconstruction of complete 3D morphologies. However, when labeling neurons in vivo, reconstruction of axons becomes the major challenge (Svoboda 2011), limiting in vivo-based approaches, so far, to small neuron numbers. Third, curvatures of the pia and white matter tract (WM) result in significant changes of column orientation and cortical thickness, even within a cortical area. Hence, axons that span multiple columns have to be quantified with respect to changing anatomical reference structures (Egger et al. 2012).

We overcame these limitations by combining cell-attached recording/labeling in rat vS1 in vivo (de Kock et al. 2007; Narayanan et al. 2014) with custom-designed high-resolution 3D reconstruction technologies (Oberlaender et al. 2007; Dercksen et al. 2014) and integration of morphologies into an accurate 3D model of the vS1 circuitry (Egger et al. 2012). This enabled us to quantify morphologies labeled across layers 2–6 (L2–L6) that represent ~1% of all excitatory neurons located within a barrel column (Meyer et al. 2013). Using an objective classification scheme, we found that our sample comprises 10 dendritic cell types, which resemble all known morphological classes reported for excitatory neurons in rat vS1 to date (Feldmeyer et al. 2013). Furthermore, we show that the dendritic cell type predicts the neurons' IC axon projection pattern. Most of the axon segments projected horizontally, innervating a cortical volume that far exceeded the dimensions of the principal column (PC, i.e., containing the soma). The 3D patterns of these horizontal axons gave rise to 3 general rules by which cortical barrel columns communicate. The most striking rule arose from asymmetrical axons, with projections along columns of the same row (i.e., adjacent whiskers along the anterior–posterior axis along the snout) exceeding those along the arc (orthogonal to the row) and vice versa. Projections along the arc originated from cell types with somata in L3, L4, L5, and L6, but were confined to [supra-]granular L1–4. In contrast, projections along the row were exclusive to infragranular L5–6, but again arose from cell types with somata located L2, L4, and L6.

Thus, cell type- and target layer-specific IC axons subdivide the cortical sheet of vS1 into 2 orthogonal horizontal strata, a layout that mirrors the organization of the facial whiskers into rows and arcs, and that is more effective and robust for coding 2-whisker inputs (Ego-Stengel et al. 2005) compared with previous models of transcolumnar communication.

Materials and Methods

Animal Preparation

All experiments were carried out in accordance with the Dutch law after evaluation by a local ethical committee at the VU University Amsterdam, The Netherlands, and with the animal welfare guidelines of the Max Planck Society. All procedures have been described in detail previously (de Kock et al. 2007; Narayanan et al. 2014). Briefly, Wistar rats (P25–P45, m/f, Charles River) were anesthetized with isoflurane and subsequently with urethane by intraperitoneal injection. The depth of anesthesia was assessed by monitoring pinch withdrawal, eyelid reflexes, and vibrissae movements. Throughout the experiment, the animal's body temperature was maintained at 37.5 ± 0.5°C by a heating pad.

In vivo Labeling

In vivo cell-attached recordings and Biocytin fillings have been described in detail previously (Pinault 1996; Narayanan et al. 2014). Briefly, pipettes were filled with normal rat ringer supplemented with 2% Biocytin. The pipette was advanced in 1 µm steps to locate single neurons, which was indicated by an increase in electrode resistance (unbiased sampling, irrespective of spiking activity). At this stage, the action potential (AP) waveforms were recorded. Subsequently, the pipette was advanced until the resistance was 25–35 MΩ and APs had an amplitude of 3–8 mV in order to obtain optimal juxtasomal filling conditions.

Juxtasomal Biocytin filling was performed by applying square pulses of positive current while gradually increasing the current in steps of 0.1 nA and monitoring the AP waveform and frequency. The membrane opening was indicated by a sudden increase in AP frequency. Filling sessions were repeated to obtain high quality axon fillings.

Histology

Animals were transcardially perfused with 0.9% saline followed by 4% paraformaldehyde (PFA). Brains were removed and post-fixed with 4% PFA for 24 h, transferred to 0.05 M phosphate buffer and stored at 4°C. One hundred micrometer thick vibratome sections were cut tangential to vS1 (45° angle) ranging from the pial surface to the WM. Sections 6–12 containing the granular part of cortex were processed for Cytochrome-C oxidase staining in order to better visualize barrel contours (Wong-Riley 1979). All sections were treated with avidin–biotin (ABC) solution and subsequently neurons were identified using the chromogen 3,3′-diaminobenzidine tetrahydrochloride (DAB) for post hoc reconstruction procedures (Horikawa and Armstrong 1988). Selection criteria for reconstructions were adequate labeling across all serial sections and sufficient cytochrome-C signals to reconstruct the barrel/septum pattern.

3D Morphological Reconstructions

In total, $n = 153$ in vivo-labeled neuron morphologies were analyzed in this study. Of these, $n = 79$ contained soma and dendrites, and $n = 74$ contained soma, dendrites, and axon. All neuron morphologies containing soma and dendrites, as well as 21 neuron morphologies containing soma, dendrites, and axon, have been reported previously (Egger et al. 2008; Bruno et al. 2009; Oberlaender et al. 2011, 2012) but in different context. Analysis of horizontal axonal projections and integration in the vS1 model were not performed for any of the previously reported morphologies. Neuronal structures were traced manually using Neurolucida software (MicroBrightfield, Williston, VT; $n = 78$ reconstructions with soma and dendrites, and $n = 11$ reconstructions with soma, dendrites, and axon), or automatically extracted ($n = 64$) from image stacks using a previously reported and validated automated tracing software (Oberlaender et al. 2007). 3D image stacks of up to 5 mm × 5 mm × 0.1 mm were acquired in vS1 at a resolution of 0.092 μm × 0.092 μm × 0.5 μm per voxel (i.e., at 100× magnification, numerical aperture 1.4). Manual proof-editing of individual sections and automated alignment across sections were performed using custom-designed software (Dercksen et al. 2014). Pia, barrel, and WM outlines were manually drawn on low resolution images (4×).

Registration of Neuron Morphologies

All neurons were registered into an average geometrical model of rat vS1. This model was based on reconstruction of the 3D geometry of the pial surface, the WM and the locations, circumferences, and orientations of 24 barrel columns from 12 Wistar rats (Egger et al. 2012). The origin of the coordinate system was set at the center of the D2 barrel in L4. The z-axis pointed dorsally, parallel to the vertical barrel column axis; the x-axis laterally toward the center of the D3 barrel within the same whisker row (Egger et al. 2012). Registration was performed by matching corresponding anatomical landmarks (pial surface, WM surface, and the L4 barrels) between the neuron reconstruction and the average vS1 model and calculating an optimal transformation of the neuron morphology that corrected for varying slicing orientations and tissue shrinkage.

Dendrite/Axon Length Measurements and Row/arc/depth Profiles

Dendrite profiles were calculated after registration to the D2 column using custom-written routines (Dercksen et al. 2014). The length density was calculated in 50 μm steps along the z-axis. Axon depth profiles and length values were calculated for each neuron after registration to the PC using custom-written software. For each axon segment, the depth below the pia, laminar location (i.e., within supragranular L1–3, granular L4, infragranular L5–6; s–g–i) as well as the horizontal location (i.e., within the PC, surrounding columns (SC), the septa between them or outside vS1) was determined and its length added to the appropriate 50 μm bin of the depth profile and to the respective laminar/horizontal axon length value. Axon profiles along the row and arc were calculated after registration to the D2 column using custom-written routines (Dercksen et al. 2014). The length density was calculated in 50 μm steps along the x-/y-axis, respectively, which are oriented parallel to the D-row/arc-2 in the average barrel cortex model.

Dendritic Cell Type Assignment

Dendritic cell types were determined based on 22 morphological, topological, and reference-frame-dependent features that were determined for each dendrite reconstruction after registration to the D2 column (Table 1 and Supplementary Fig. S1). In the first step, all cells were grouped according to their mutual distances in the 22-dimensional feature space using the OPTICS algorithm (Ankerst et al. 1999). This revealed a clear separation between supragranular/granular (in the following refered to as *[supra-]granular*) and infragranular neurons, except for one neuron, which was subsequently grouped with the [supra-]granular neurons based on its laminar soma location. Next, [supra-]granular neurons were sorted using OPTICS in 3D feature spaces that have previously been shown to separate supragranular and granular cell types, respectively (Oberlaender et al. 2012). Neurons that could be unambiguously assigned to the supragranular or granular feature spaces were not considered in the other feature space anymore. This procedure was iteratively repeated until a robust set of supragranular (4 groups comprising 38 neurons) and granular (4 groups comprising 36 neurons) groups was determined, while a minority of neurons ($n = 16$) could not be unambiguously assigned. Infragranular neurons were sorted using OPTICS in a 21-dimensional feature space which has previously been shown to separate between infragranular cell types (Oberlaender et al. 2012). This sorting revealed 4 infragranular neuron groups comprising 56 neurons. For 7 neurons, unambiguous assignment to one of these groups was not possible. In order to also assign ambiguous neurons to one of the groups, we calculated their distances to each group. The distance d_k of a neuron to group k was calculated as follows:

$$d_k = \sqrt{(\vec{f} - \vec{\mu_k})^T C_k^{-1} (\vec{f} - \vec{\mu_k})}.$$

Here, $\vec{f}$ is the feature vector of the neuron, $\vec{\mu_k}$ is the mean feature vector of group k, and C_k^{-1} is the inverse covariance matrix of group k in the respective feature space. Intuitively, this is the distance of the neuron to the mean of group k in the feature space in units of standard deviations of each feature of group k. Because

Table 1 Soma-dendritic (top) and axonal (bottom) features (mean ± SD) used for assignment of excitatory cell types

Dendritic features	L2py ($n = 16$)	L3py ($n = 30$)	L4sp ($n = 15$)	L4ss ($n = 22$)	L4py ($n = 7$)	L5st ($n = 18$)	L5tt ($n = 16$)	L6cc ($n = 11$)	L6ct ($n = 13$)	L6inv ($n = 5$)
Reference frame										
Soma in s–g–i	s: 16	s: 16; g: 14	s: 4; g: 10; i: 1	g: 21; i: 1	g: 7	i: 18	i: 16	i: 11	i: 13	i: 5
Soma depth (μm)	293 ± 97	510 ± 120	618 ± 125	758 ± 95	677 ± 40	1098 ± 98	1165 ± 78	1377 ± 86	1492 ± 122	1505 ± 85
All dendrites										
Length (μm)	8472 ± 1843	7092 ± 2412	4040 ± 662	3117 ± 1011	5606 ± 1885	7378 ± 1680	14 729 ± 3391	7113 ± 1587	6127 ± 1186	8434 ± 1732
BB (10^7 μm^3)	5.53 ± 1.05	4.43 ± 2.02	2.62 ± 1.61	0.97 ± 0.54	3.56 ± 0.54	12.3 ± 3.03	24.8 ± 10.1	9.01 ± 3.43	4.63 ± 1.80	12.4 ± 1.79
BB hori. extent (μm)	575 ± 87	383 ± 57	337 ± 53	266 ± 41	342 ± 21	456 ± 55	613 ± 119	470 ± 46	328 ± 55	513 ± 58
Branch points	62 ± 15	44 ± 17	23 ± 5	26 ± 15	37 ± 12	35 ± 11	86 ± 23	35 ± 7	38 ± 8	44 ± 11
Avg branch order	4 ± 1	3 ± 1	2 ± 1	2 ± 1	3 ± 2	3 ± 1	6 ± 2	3 ± 1	5 ± 2	5 ± 1
Max branch order	11 ± 3	10 ± 3	5 ± 2	5 ± 2	9 ± 5	7 ± 2	17 ± 5	8 ± 2	15 ± 4	14 ± 2
Avg endp.-soma (μm)	149 ± 17	172 ± 37	133 ± 21	109 ± 15	156 ± 29	260 ± 36	399 ± 91	187 ± 17	213 ± 40	221 ± 16
Max endp.-soma (μm)	368 ± 45	443 ± 130	311 ± 137	190 ± 53	488 ± 27	1031 ± 102	1126 ± 77	612 ± 168	750 ± 135	616 ± 101
Sum endp.-soma (μm)	10 473 ± 2756	8992 ± 4048	4013 ± 991	3315 ± 1423	7140 ± 2818	11 217 ± 2993	38 218 ± 13 114	7653 ± 1600	9591 ± 2924	11 172 ± 2422
CMS-soma (μm)	63 ± 14	61 ± 31	25 ± 12	36 ± 14	68 ± 52	138 ± 38	296 ± 100	39 ± 19	149 ± 42	65 ± 51
Apical dendrite										
Length (μm)	4310 ± 1071	3269 ± 1629	1210 ± 474		2578 ± 903	3206 ± 823	7946 ± 1589	2716 ± 1103	3744 ± 796	3275 ± 827
BB(10^7 μm^3)	3.68 ± 0.83	2.47 ± 1.42	0.68 ± 0.44		2.09 ± 0.52	6.19 ± 2.86	19.5 ± 9.45	4.20 ± 2.61	2.85 ± 1.43	5.02 ± 2.38
BB hori. extent (μm)	555 ± 87	328 ± 67	201 ± 57		296 ± 36	343 ± 74	578 ± 129	360 ± 84	271 ± 51	417 ± 111
BB vert. extent (μm)	255 ± 70	447 ± 132	319 ± 149		492 ± 39	1052 ± 102	1130 ± 80	629 ± 186	760 ± 144	576 ± 75
CMS-soma (μm)	137 ± 34	164 ± 66	106 ± 48		162 ± 49	379 ± 76	569 ± 136	163 ± 51	263 ± 78	202 ± 50
Basal dendrites										
Length (μm)	4162 ± 1128	3823 ± 1131	2772 ± 573		3027 ± 1542	4172 ± 1209	6783 ± 2451	4398 ± 1072	2383 ± 568	5159 ± 1431
BB (10^7 μm^3)	1.31 ± 0.5	1.61 ± 0.6	1.17 ± 0.49		1.18 ± 0.44	2.57 ± 1.00	4.49 ± 2.27	3.30 ± 1.04	0.85 ± 0.42	5.23 ± 1.82
BB hori. extent (μm)	332 ± 43	354 ± 38	322 ± 49		323 ± 36	439 ± 60	541 ± 93	454 ± 52	316 ± 56	468 ± 37
BB vert. extent (μm)	232 ± 56	259 ± 74	225 ± 65		224 ± 62	262 ± 58	289 ± 75	319 ± 55	163 ± 38	528 ± 190
Branch points	31 ± 8	23 ± 9	16 ± 5		18 ± 9	21 ± 8	39 ± 15	22 ± 6	14 ± 4	26 ± 8
Axonal features	$n = 9$	$n = 14$	$n = 5$	$n = 9$	$n = 4$	$n = 5$	$n = 7$	$n = 6$	$n = 11$	$n = 4$
Branch points	214 ± 130	181 ± 72	185 ± 34	177 ± 88	218 ± 68	216 ± 35	88 ± 55	215 ± 115	48 ± 28	232 ± 111
BB (10^9 μm^3)	5.90 ± 0.63	6.29 ± 6.80	3.38 ± 1.30	1.56 ± 0.66	6.48 ± 5.11	7.72 ± 3.15	3.48 ± 1.82	13.9 ± 9.03	1.42 ± 1.52	20.8 ± 13.3
Length (mm)										
Total	42.73 ± 15.55	61.24 ± 24.82	68.20 ± 15.20	49.29 ± 21.38	67.34 ± 21.76	86.98 ± 5.71	26.62 ± 15.21	119.34 ± 64.40	15.64 ± 1.49	111.85 ± 42.25
In vS1	39.75 ± 15.52	49.23 ± 22.68	65.01 ± 12.09	47.64 ± 19.99	57.90 ± 20.34	78.47 ± 12.82	24.64 ± 14.23	91.36 ± 53.94	14.52 ± 9.82	83.07 ± 25.94
In PC	12.97 ± 7.87	13.12 ± 7.41	24.84 ± 6.10	29.35 ± 18.61	16.64 ± 6.62	17.60 ± 6.82	9.54 ± 4.85	12.84 ± 6.74	6.08 ± 3.31	12.83 ± 4.01
In SCs	13.13 ± 7.32	20.90 ± 12.28	20.49 ± 6.07	9.24 ± 5.28	23.17 ± 13.46	33.73 ± 8.22	8.94 ± 6.20	57.50 ± 36.43	6.00 ± 6.20	54.48 ± 21.18
In septa	13.66 ± 7.00	15.21 ± 11.24	19.69 ± 5.35	9.05 ± 2.74	18.09 ± 5.79	27.14 ± 5.85	6.16 ± 4.89	21.02 ± 14.08	2.44 ± 3.19	15.77 ± 5.07
Outside vS1	2.97 ± 2.83	12.00 ± 14.66	3.19 ± 4.46	1.65 ± 2.38	9.44 ± 13.65	8.51 ± 9.17	1.98 ± 1.97	27.98 ± 33.20	1.12 ± 0.88	28.78 ± 24.34

Continued

Table 1 Continued

Dendritic features	L2py ($n = 16$)	L3py ($n = 30$)	L4sp ($n = 15$)	L4ss ($n = 22$)	L4py ($n = 7$)	L5st ($n = 18$)	L5tt ($n = 16$)	L6cc ($n = 11$)	L6ct ($n = 13$)	L6inv ($n = 5$)
In supra vS1	27.10 ± 10.12	21.76 ± 15.75	32.58 ± 11.44	17.77 ± 9.28	23.43 ± 5.16	49.30 ± 12.65	4.20 ± 3.31	13.34 ± 9.21	0.515 ± 0.03	5.38 ± 4.25
In gran vS1	3.24 ± 2.61	10.80 ± 4.36	22.12 ± 3.03	20.91 ± 9.39	16.01 ± 8.09	9.73 ± 3.35	3.10 ± 3.22	14.85 ± 11.37	1.59 ± 0.56	2.63 ± 1.23
In infra vS1	9.42 ± 6.62	16.67 ± 10.34	10.31 ± 5.68	8.96 ± 5.62	18.46 ± 14.35	19.44 ± 3.61	17.35 ± 8.63	63.17 ± 40.32	12.42 ± 9.14	75.06 ± 26.26
In supra PC	7.85 ± 5.23	4.77 ± 3.65	9.69 ± 3.42	10.03 ± 7.56	6.14 ± 1.93	7.16 ± 3.62	1.44 ± 1.29	2.35 ± 1.66	0.07 ± 0.05	1.41 ± 2.08
In gran PC	1.48 ± 1.71	3.50 ± 2.39	9.47 ± 2.53	13.78 ± 8.97	5.02 ± 4.11	2.46 ± 0.96	1.36 ± 1.57	1.94 ± 1.89	0.73 ± 1.02	0.68 ± 0.89
In infra PC	3.64 ± 2.47	4.85 ± 3.21	5.69 ± 2.83	5.53 ± 3.65	5.48 ± 2.60	7.99 ± 2.93	6.75 ± 3.39	8.55 ± 3.80	5.28 ± 290	10.73 ± 2.23

Note: Dendritic features: (1) laminar location of the soma in supra- (s), granular (g) or infragranular layers (i); (2) pia-soma distance along the vertical cortex axis after registration to the D2 barrel column (soma depth); (3) total dendrite path length (length); (4) volume of the bounding box around all dendrites (BB); (5) lateral extent of the dendrite BB (hori. extent); (6) number of bifurcations (branch points); (7) depth of the dendritic tree averaged across all dendrites (avg branch order); (8) deepest branch order (max branch order); (9) direct Euclidean distance between dendrite ending points and soma, averaged across all ending points (avg endp.-soma); (10) maximal ending point to soma distance (max endp.-soma); (11) sum of all endpoint to soma distances (sum endp.-soma); (12) Euclidean distance between the dendrites center of mass and the soma (CMS-soma); (13) path length of the apical dendrite; (14) volume of the bounding box around the apical dendrite; (15) lateral extent of the apical dendrite BB; (16) vertical extent of the apical dendrite BB (verti. extent); (17) Euclidean distance between the apical dendrite's center of mass and the soma; (18) path length of basal dendrites; (19) volume of the bounding box around all basal dendrites; (20) lateral extent of the basal dendrite BB; (21) vertical extent of the basal dendrite BB; (22) number of bifurcations along basal dendrites. Axonal features: (1) number of bifurcations along axon (branch points); (2) bounding box volume around axon (BB); (3) total path length of axon; (4) path length in barrel cortex (in vS1); (5) path length in principal column (in PC); (6) path length in columns surrounding the PC (in SCs); (7) path length in the septa (i.e., between columns); (8) path length outside vS1 (i.e., in dysgranular cortex); (9–11) path lengths in supragranular L1–3, granular L4 and infragranular L5–6; (12–14) path lengths in supragranular L1–3, granular L4, and infragranular L5–6 within the PC.

[supra-]granular and infragranular feature spaces have different dimensions (3 vs. 21), we converted these distances into a comparable probability space. Assuming that neuron features are normally distributed around the mean of each group, we converted each distance d_k into a probability p_k using the cumulative distribution function F of the χ^2 distribution (i.e., p_k is the probability of finding a neuron at a distance equal to or more than d_k from group k):

$$p_k = 1 - F(d_k^2, \mathrm{DOF}_k).$$

Here, DOF_k are the degrees of freedom of group k. For [supra-]granular neurons, this was equal to the dimensions of the feature space. For infragranular neurons, this was equal to the rank of the covariance matrix C_k, because infragranular groups consisted of less neurons than the dimensionality of the infragranular feature space. This value was compared with the values of p_k computed for all other groups and the neuron was assigned to the group with the highest value of p_k, and the probability of the neuron belonging to group k was calculated as

$$P(k) = p_k / \sum_{\text{groups } i} p_i$$

Finally, 3 groups in supragranular layers were merged to L3py, 2 groups in the granular layer were merged to L4sp and one neuron group in infragranular layers was split into the L6cc and L6inv based on common dendritic/axonal vertical projection profiles.

3D Average Model of Axon Distributions in rat vS1

The procedures to generate cell type-specific axon distributions within the average model of vS1 have been described in detail previously (Egger et al. 2014). Briefly, the number and 3D distribution of all excitatory neuron somata in rat vS1 was measured with respect to the anatomical landmarks (Meyer et al. 2013) and then registered to the average cortex model at a resolution of $50 \times 50 \times 50\ \mu m^3$. Next, the axon morphologies were scaled up to the number of neurons of each excitatory cell type. Each excitatory neuron soma was assigned to a cell type based on the relative frequency of occurrence of different cell types at the same depth as the soma (measured in 50 μm steps). For each soma, an axon morphology of the same cell type that was registered to the column closest to the soma was then placed in the model at its registered location. These axon morphologies were converted into cell type-specific 3D bouton distributions by computing the 3D axon density for each cell type at a resolution of $25 \times 25 \times 25\ \mu m^3$ and multiplying by cell type- and target layer-specific bouton length densities.

Bouton Counting

Average bouton length densities were obtained from high-resolution images stacks (100×, NA = 1.4; $0.092 \times 0.092 \times 0.2\ \mu m^3$ voxel size; Supplementary Fig. S2) in supra-, granular, and infragranular layers. Horizontally projecting axons were chosen for analysis. Bouton length densities were determined by manually marking the 3D location of each bouton along the reconstructed axons and measuring the respective path lengths between the marked boutons. Boutons were assigned as *en passant* or *terminal*. En passant boutons were identified as prominent and approximately spherical swellings along axonal branches, without definition of a minimal radius. Terminal boutons were identified as prominent and approximately spherical swellings located at the end of short axonal branches. Swellings were assigned as boutons only if the swellings were visible in all 3 image planes

(see examples in Supplementary Fig. S2F). Measurements were performed for $n = 11\,386$ boutons from axonal segments in $n = 22$ different rats (Supplementary Table S1).

Bouton Density Row/arc Profiles

Bouton density profiles for each cell type along the C-row were calculated from the 3D bouton distribution of vS1 by summing up all $25 \times 25 \times 25\ \mu m^3$ voxels that were closest to any of the 4 C-row barrel columns in 25 μm steps along the *x*-axis separately in supra-, granular, and infragranular layers, and dividing by the volume of these voxels. In the same way, bouton density profiles along arc-2 were calculated along the *y*-axis. Differences between bouton densities in columns and septa were tested as follows: First, for each layer (s–g–i) we calculated the average bouton density of all 25 μm bins for columns C1, C2, and C3 and for septa between C1/C2, C2/C3, and C3/C4, respectively. We then performed a 2-tailed *t*-test to determine whether average bouton densities were different between columns and septa. The same calculation was performed for columns along the arc (B2, C2, D2) and the septa between B2/C2, C2/D2, and D2/E2. This coarse measure (i.e., each column and septum was condensed to a single density value, respectively) revealed significant ($P < 0.05$) and trend level ($P < 0.1$) differences between columnar and septal bouton densities for some cell types and target layers. Second, for each layer (s–g–i), we assigned each 25 μm bin of the bouton density profiles to column or septum and performed a 2-tailed *t*-test between column-related and septum-related bins with significance level set at 0.05. This measure was used to assign the cell type- and target layer-specific bouton profiles to the columnar/septal, patterned or unpatterned projection rules. A single asterisk in Figure 8C,F thus denotes cell types that had significant differences between columnar and septal densities as determined by our second measure. Two asterisks denote cell types where these differences were already significant or at trend level using our coarse measure. Qualitatively, 2 asterisks denote cell types whose columnar/septal density differences were more prominent compared with those with one asterisk.

RESULTS

Classification of Axo-Dendritic Excitatory Cell Types in Rat vS1

Dendritic and axonal branches of individual in vivo-labeled excitatory neurons, as well as outlines of the pia, WM, and L4 barrels were traced within consecutive vibratome sections (Fig. 1A,B). The outlines of these reference structures were used to register morphologies into the vS1 model (Egger et al. 2012). This approach hence allowed quantifying 3D dendritic ($n = 153$) and axonal ($n = 74$) projection patterns, at single neuron levels, with respect to the laminar, columnar, and somatotopic organization of vS1 (Fig. 1C,D).

To objectively identify morphological cell types within this sample, we developed a multistep classification approach (Supplementary Fig. S1 and Table 1). The first step subdivided our sample into 2 major soma-dendritic classes: neurons with somata located either above (supragranular L2–3) and within (granular L4) the barrel ($n = 90$), or below the barrel (infragranular L5–6, $n = 63$). Neurons with somata in L2–4 were termed *[supra-]granular*. The second step revealed 5 cell types within the [supra-] granular population (Fig. 2A,B), in the following referred to as L2, L3, L4 pyramids (L2py, L3py, L4py), L4 star-pyramids (L4sp) and L4 spiny-stellates (L4ss, see Table 2 for a list of all abbreviations). Plotting the first 2 principal components of the respective feature spaces illustrated the validity of our approach, where soma-dendritic cell types formed disjoint clusters (Fig. 2C).

We determined axonal parameters for each [supra-]granular neuron ($n = 41$) and grouped these features by the respective soma-dendritic cell type. One of several features (Table 1) that discriminated well between axonal cell types was the relative proportion of axon each neuron projected towards supragranular (s), granular (g), and infragranular (i) layers. To visualize these measures, we converted the respective relative proportions into 2 axon indices (Fig. 2D). Plotting the mean and SDs of these indices for the respective soma-dendritic cell types illustrated that [supra-]granular neurons displayed axonal projection patterns that were similar within, but significantly different between soma-dendritic cell types.

We repeated this classification approach for the infragranular neurons ($n = 63$) and obtained 5 additional soma-dendritic cell types (Fig. 3A,B), in the following referred to as L5 slender-tufted (L5st), L5 thick-tufted (L5tt), L6 corticocortical (L6cc), L6 corticothalamic (L6ct), and L6 inverted (L6inv) pyramids. The 5 infragranular cell types formed disjoint clusters in the soma-dendritic (Fig. 3C) and axonal (Fig. 3D, $n = 33$) feature spaces. Because the dendritic morphology predicted the axonal projection pattern of the respective neuron, we consider soma-dendritic and axonal cell types as the same and refer to them as axo-dendritic cell types (for a gallery of all cells, see Supplementary Figs S3–S5).

The Majority of IC Axons Project Beyond Columnar Borders

Somata of all axo-dendritic cell types intermingled within and across cytoarchitectonic layers (Fig. 4A and Table 1). However,

Table 2 List of abbreviations

TC	Thalamocortical
IC	Intracortical
vS1	Vibrissal part of rat primary somatosensory cortex (barrel cortex)
S1	Primary somatosensory cortex
V1	Primary visual cortex
A1	Primary auditory cortex
M1	Primary motor cortex
PFC	Prefrontal cortex
PC	Principal barrel column
PCC	Principal barrel column center
SC	Surrounding barrel column
WM	White matter tract
L1–6	Cytoarchitectonic cortical layers 1–6
Supragranular (s)	Above the barrel (L1–3)
granular (g)	Inside the barrel (L 4)
Infragranular (i)	Below the barrel (L5–6)
[supra-]granular	Above and inside the barrel (L1–4)
L2py	L2 pyramidal neuron
L3py	L3 pyramidal neuron
L4py	L4 pyramidal neuron
L4sp	L4 star-pyramidal neuron
L4ss	L4 spiny-stellate neuron
L5st	L5 slender-tufted pyramidal neuron
L5tt	L5 thick-tufted pyramidal neuron
L6cc	L6 corticocortical pyramidal neuron
L6ct	L6 corticothalamic pyramidal neuron
L6inv	L6 inverted pyramidal neuron
OS	Orthogonal strata
SymCols	Symmetric columns
RowCols	Rowish columns

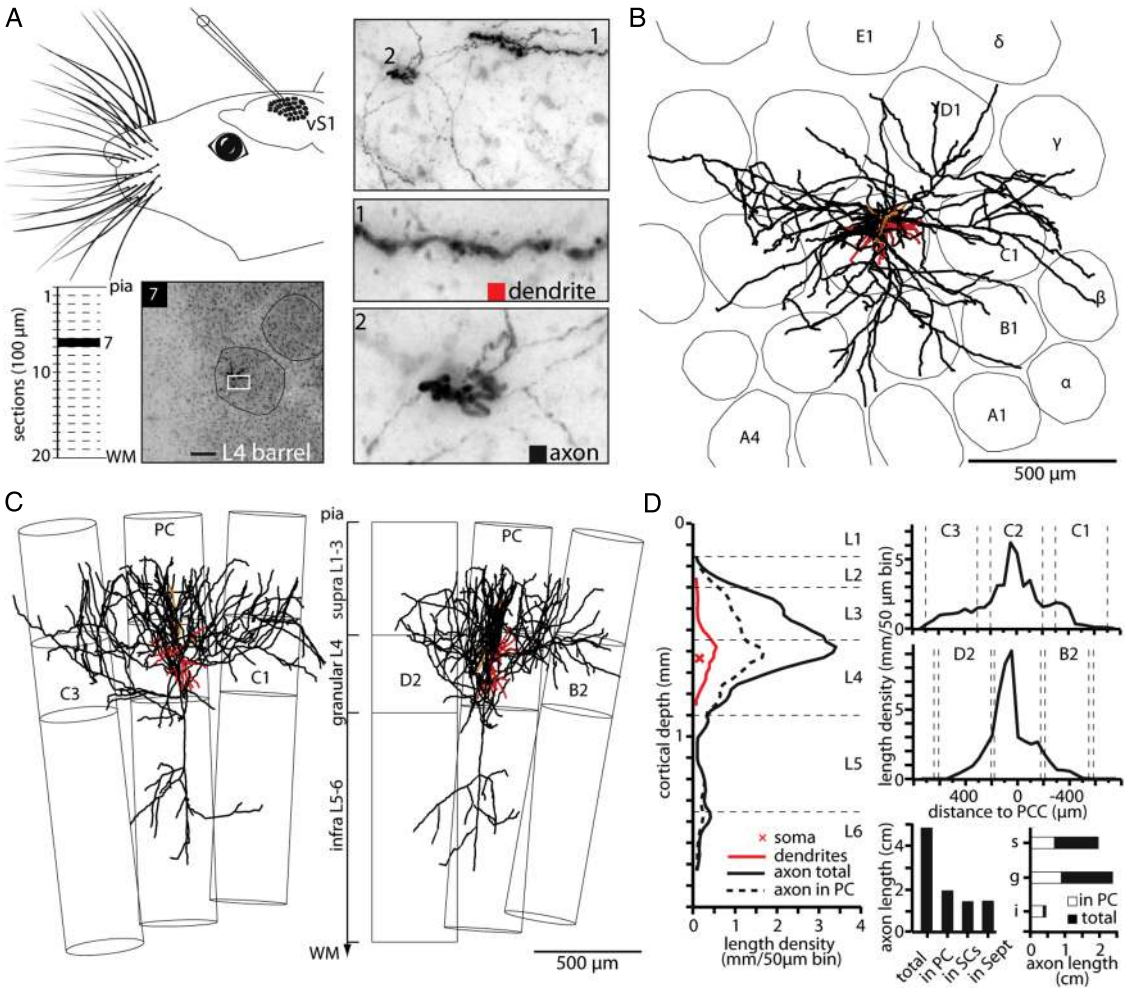

Figure 1. 3D reconstruction of in vivo-labeled axons and dendrites. (*A*) Individual neurons in rat vS1 are labeled with Biocytin using cell-attached recordings (top left). Post hoc slicing into consecutive vibratome sections allows recovering labeled neurons with respect to cytoarchitectonic landmarks, such as pia, WM and barrel circumferences (bottom left). Projection image of section 7 of 20. Zoom into projection image (white box, top right) reveals dendritic (1) and axonal (2) branches. Zoom in at locations 1 and 2 reveals spines (center right) and boutons (bottom right). (*B*) Top view (tangential to vS1) of 3D reconstructed neuron shown in panel *A*, with respect to somatotopic organization of vS1 into whisker rows (*A*–*E*) and arcs (1–4). (*C*) Semi-coronal views of neuron in panel *A*,*B* along whisker row (left) and arc (right). (*D*) Quantitative analysis of vertical (left) and horizontal (right) axonal innervation of neuron shown in panel *A*–*C*. Left panel: the soma is located in L4 and the apical dendrite extends toward L2 (lacking an apical tuft) rendering the exemplary neuron as a L4sp. Cytoarchitectonic layer borders (dashed lines) are based on changes in soma density along the vertical cortex axis, as reported previously (Meyer et al. 2010). Right panel: axon segments extended asymmetrically beyond the dimensions of the PC, projecting wider along the row than along the arc. Relative fraction of axon in/outside the PC depended on the target layer (bottom right, s: L1–3, g: L4, i: L5–6).

within our sample, somata of [supra-]granular and infragranular cell types did not overlap, rendering the L4/5 border as a cytoarchitectonic landmark that divides cortex into 2 major *cell type strata* (i.e., L2–4 and L5–6), with each stratum containing 5 axo-dendritic excitatory cell types whose somata partially intermingle.

Consequently, we quantified vertical (Fig. 4*A*) and horizontal (Fig. 4*B*,*C*) dendrite/axon innervation profiles in a cell type-specific rather than a layer-specific manner. Axons of L2py were largely confined to supragranular layers, reaching peak densities within L2. Most axon of L2py projected beyond the dimensions of the PC, innervating surround columns (SCs) and septa between them. Axons of L3py innervated SCs throughout L1–5, reaching peak densities at the border between L2 and L3, and in the center of L5. L4sp axons were largely confined to the [supra-]granular stratum of the PC and SCs, reaching peak densities in L3. Axons of L4py resembled those of L3py, but terminated within L2 (i.e., L3py axons reached L1). Discriminating them from the other 4 [supra-]granular cell types, L4ss axons were largely confined to the PC, where they innervate the [supra-]granular stratum homogeneously between L2–4. L5st axons densely innervated all SCs in supragranular layers and remained more confined to the PC in L5. Axonal projections of L5tt were sparse and largely confined to L5, where they innervate SCs. L6cc had the most elaborate axonal projections, innervating all SCs at all cortical depths, reaching peak densities at the L5/6 border. In contrast, L6ct had the least amount of IC axon of all cell types, which was mostly confined to L5/6 within the PC. L6inv axons were as elaborate as those of conventional L6cc, but remained largely confined to L5/6.

Finally, we estimated the degree by which in vitro studies may have underestimated axonal path lengths of the respective cell types (axonal length ratio in vivo/vitro: L2py: 2, L3py: 5 [Feldmeyer et al. 2006]; L4sp/ss/py: 11 [Lubke et al. 2000]; L5st: 10, L5tt: 4 [Brown and Hestrin 2009]; L6ct: 4, L6cc/inv: 24 [Kumar and Ohana 2008]). The in vitro studies were however performed in juvenile rats (around postnatal days 14–21), whereas our data

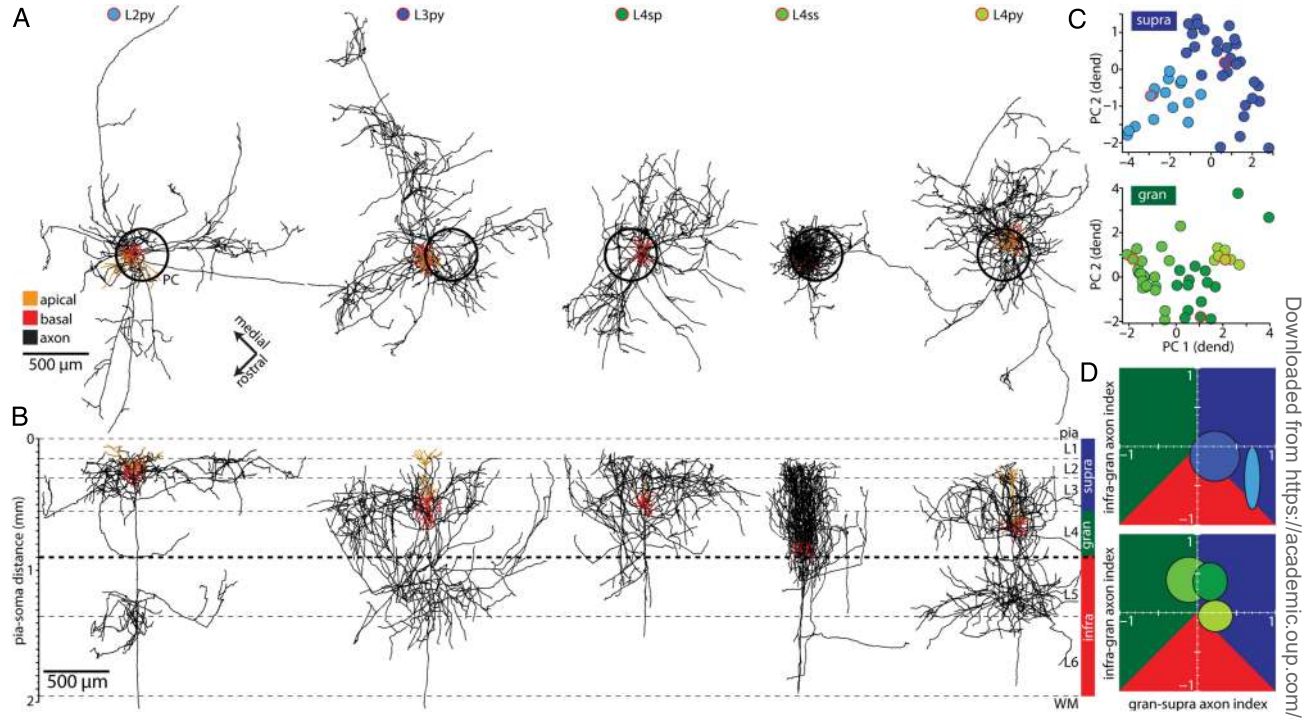

Figure 2. Axo-dendritic cell types in the [supra-]granular stratum. (*A*) Top view onto exemplary morphologies of the 5 excitatory cell types located in L2–4. (*B*) Semi-coronal view along the arc of the morphologies shown in panel *A*. Bold dashed line represents the L4/5 border. (*C*) Raster plots of the first 2 principal components (PCs) of soma-dendritic features that discriminated between [supra-]granular cell types. Red outlined circles represent the exemplary neurons in panel *A*,*B*. (*D*) Analyses of cell type-specific axonal features. The horizontal and vertical axes refer to the relative proportion of axon in granular/supragranular and infragranular/granular layers, respectively. The *gran-supra axon index* (*g-s*) is −1 or +1 if all axon was within L4 or L1–3, respectively. The *infra-gran axon index* (*i-g*) is −1 or +1 if all axon was within L5–6 or L4, respectively. Ellipses represent mean ± SD of the respective 5 [supra-]granular soma-dendritic cell types. Background colors (as in panel *B*) indicate where most axon of a respective cell type was found. Ellipses were largely disjoint. Thus, neurons grouped by soma-dendritic features shared cell type-specific axonal morphologies.

represents neurons in young adults (postnatal days 25–45). Our estimate may thus be regarded as an upper limit for how much axon is cut off from individual neurons in in vitro preparations of typical slice thicknesses (~350–400 µm).

Transcolumnar IC Axons are Asymmetric and Target Layer-Specific

With the exception of L4ss, all cell types projected most of their axon beyond the dimensions of the PC. We thus calculated the lateral axon extents (at 50 µm resolution) for each cell type along the row (Fig. 4*B*) and arc (Fig. 4*C*), respectively. Lateral extents were in general asymmetric (Fig. 4*D*), with axons spreading on average (across all cell types) 12 ± 6% wider along the row than along the arc. Furthermore, the relative proportion of axon within and outside the PC deviated for the respective target layers (i.e., L1–3: supragranular, L4: granular, L5–6: infragranular (s–g–i); Fig. 4*E*).

These cell type- and target layer-specific horizontal extents were further illustrated by calculating 3D surfaces around all dendrites and all IC axons from each cell type, respectively (i.e., dendrite/axon projection volumes, Fig. 5). The dendrite projection volume of each cell type, with the exception of the L5st and L5tt pyramids, was largely restricted to the stratum containing the respective somata (i.e., dendrites of [supra-]granular and infragranular cell types remained within the respective stratum) and to the dimensions of the PC (Oberlaender et al. 2012). In contrast, the axon projection volumes of all cell types extended vertically to both strata and horizontally into SCs. Combining these cell type-specific axon projection volumes resulted in a 3D surface (Fig. 6*A*) that resembled the shape of an hourglass (Fig. 6*B*), where horizontal axon extents in supra- and infragranular layers exceeded those in the granular layer (Fig. 6*C*). The hourglass-shaped volume is in the following referred to as *IC-unit*. The IC- unit of vS1 comprised a volume of ~3 × 3 barrel columns (IC-unit: 1.63 mm^3 vs. barrel column: 0.24 mm^3 (Wimmer et al. 2010)).

Integration in a vS1 Model Reveals Rules of Transcolumnar Projections

The shape of the IC-unit of vS1 resembled the volume as revealed by bulk injections previously (Bernardo et al. 1990). Our analyses at cellular resolution revealed however that axons within the IC-unit had specific horizontal projections there were asymmetric depending on the cell type and target layer (Fig. 7). To investigate the organizational principles underlying the various horizontal patterns within the IC-unit, we developed a more precise 3D analysis routine. Because of substantial cortical curvatures across vS1, mutually tilted barrel columns result in depth-, column-, row-, and arc-specific septa sizes and orientations (Egger et al. 2012). To minimize measurement errors of axonal asymmetry, we thus reregistered (Egger et al. 2012) all morphologies to each of the 24 major barrel columns (A1–E4, α–δ). Furthermore, to compensate for cell type-specific differences in the axonal bouton distributions, we converted the morphologies into 3D bouton densities by multiplying axonal lengths with bouton length densities, measured for the respective cell type and target layer (Supplementary Fig. S2 and Table S1). This procedure is illustrated for L4ss (Fig. 8*A*) and L6cc (Fig. 8*D*; Supplementary Fig. S6 for all cell types).

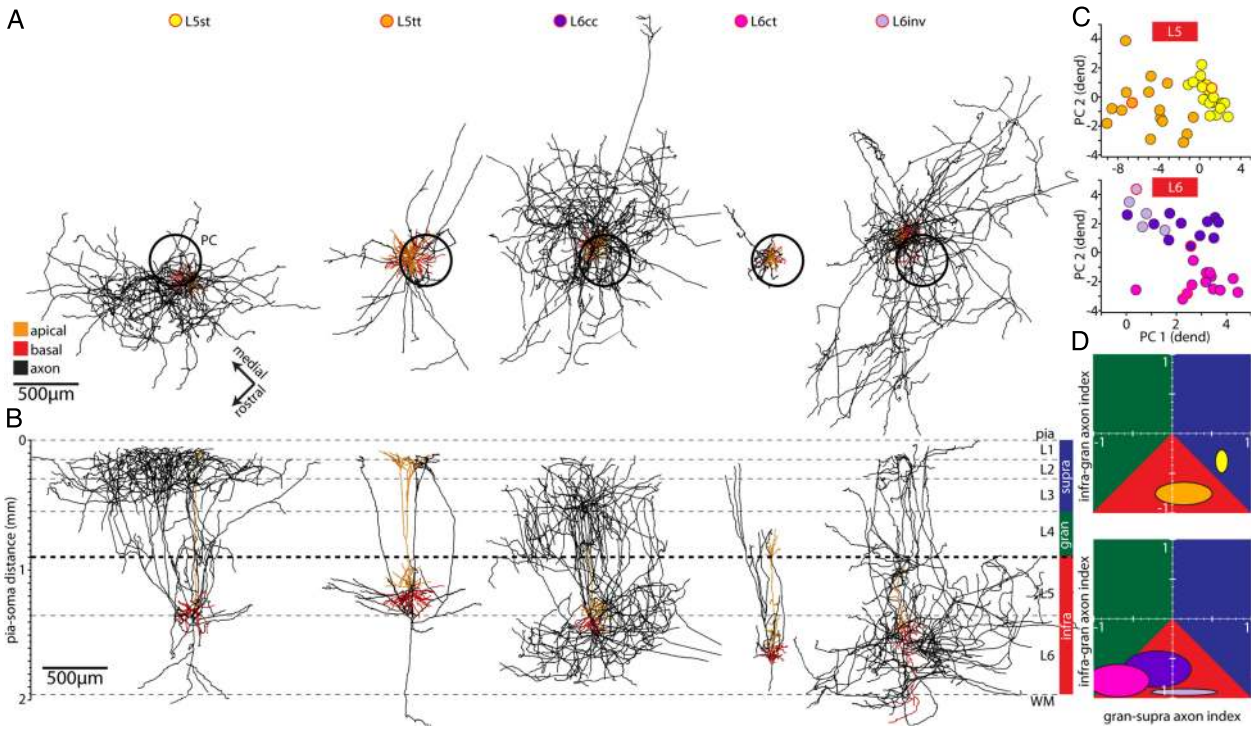

Figure 3. Axo-dendritic cell types in the infragranular stratum. (*A*) Top view onto exemplary morphologies of the 5 excitatory cell types located in L5–6. (*B*) Semi-coronal view along the arc of the morphologies shown in panel *A*. (*C*) Raster plots of the first 2 PCs of soma-dendritic features that discriminated between infragranular cell types (*D*). Analyses of cell type-specific axonal features (as in Fig. 2). As for the [supra-]granular cell types, ellipses were disjoint indicating that dendrite and axon morphologies were cell type-specific.

We then calculated 1D bouton density profiles along the row and arc for each cell type and target layer (s–g–i), respectively. Bouton density values of L4ss decreased in all layers from the principal column center (PCC) toward its borders, reaching minima at the centers of the septa, both along the row and the arc (Fig. 8*B*). To quantify these differences, we calculated the average density values across the C1-3 columns and respective septa for the 3 target layers (s–g–i). Along the row, L4ss bouton densities in septa were significantly lower compared with columns. Calculating the corresponding values across the B2–D2 columns (arc-2), revealed similar significant decreases in bouton densities between the columns. Such *up-and-down* horizontal projection patterns, when present along the row and arc, were termed *columnar* (Fig. 8C).

Significant differences between columnar and septal densities were, however, not always present. Depending on the cell type and target layer, septa vanished in the respective bouton profiles (Supplementary Fig. S6) either along the row (e.g., L2py in L4) or along the arc (e.g., L3py in L4). The organizational principles of such *patterned* horizontal axon projections were termed *rowish* (i.e., minima were present only along the arc) and *arcish* (i.e., minima were present only along the row), respectively (e.g., L2 axons innervate the granular layer continuously along the row, L3 axons continuously along the arc). Columnar and patterned (arcish/rowish) horizontal projections were specific for each [supra-]granular cell type and target layer (Fig. 8C). Repeating this analysis for the 5 infragranular cell types revealed 2 additional horizontal projection types. First, septa in some bouton profiles (e.g., L6cc infragranular) were neither present along the row, nor along the arc (Fig. 8E). Such symmetric horizontal projections were termed *unpatterned*. Second, some bouton density profiles reached maximal values within septa, not in columns. *Septal* horizontal patterns were exclusive to projections along rows (e.g., L5st axons in supragranular layers). As for the [supra-]granular cell types, the 3 rules of transcolumnar projections—columnar, septal, patterned (rowish/arcish) and unpatterned—were specific for each infragranular cell type and target layer (Fig. 8F).

Deconstructing the IC-unit of vS1 Reveals Orthogonal Horizontal Strata

To quantify how many boutons each cell type contributes to the vS1 circuitry, and thus how much of the IC-unit is organized by the respective horizontal and vertical axonal projections, we scaled our sample up to the total number of neurons located in vS1 ([Egger et al. 2014], Fig. 9). This allowed deconstructing the IC-unit into the relative proportions of columnar, septal, arcish, rowish, and unpatterned projections by summing the target layer-specific vertical bouton density profiles across all cell types that were assigned to the same organizational principle.

Columnar Pathways

Columnar patterns were present throughout the entire cortical depth, representing on average 45% of all projections within the IC-unit. These intracolumnar vertical pathways can be subdivided into 3 classes. First, *columnar–local* pathways comprised cell types whose axonal projections patterns remained columnar within the layer containing the respective somata (L2py in supragranular, L4ss and L4sp in granular, L5st and L6ct in infragranular layers). Second, *columnar–translaminar* pathways comprised cell types whose axons remained columnar but projected beyond the layer containing the respective somata (L4ss axons in supragranular, L3py axons in infragranular layers). Third, *septal* pathways represented on average 7% of the

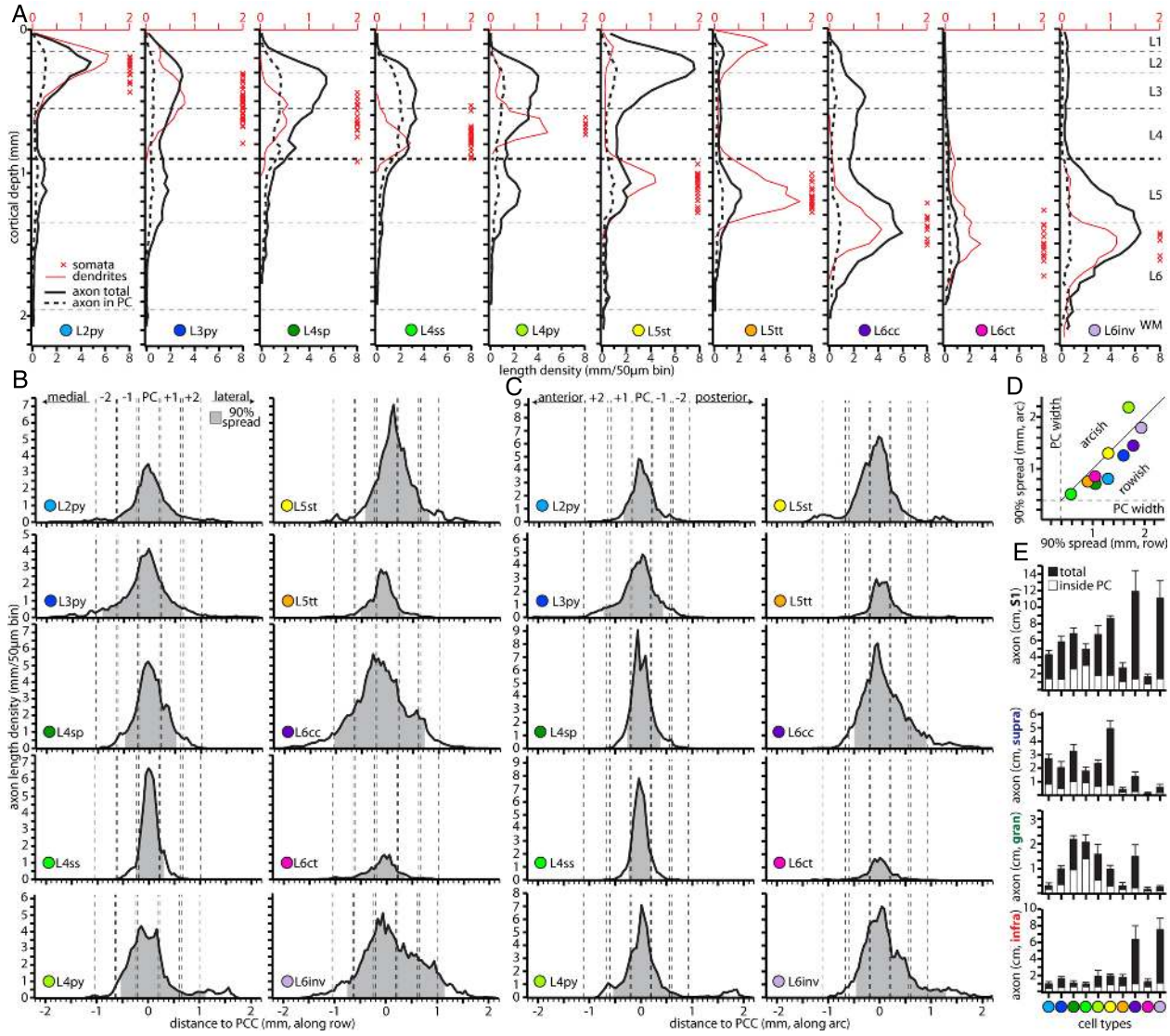

Figure 4. Cell Type-specific vertical and horizontal axon projection patterns. (*A*) 1D density profiles along vertical cortex axis of dendrites (red) and axons (black), averaged across all neurons assigned to one of the 10 excitatory cell types, respectively. Somata of multiple [supra-]granular cell types intermingled (red "×" denotes the respective soma depths below the pia), but were segregated from infragranular cell types, which also intermingled within and across cytoarchitectonic layers. Dendritic and axonal profiles were cell type-specific, with most axon projecting beyond PC dimensions (inside PC: dashed line profiles; inside vS1: solid line profiles). (*B*) 1D axon density profiles of the 10 cell types along the row extended in general beyond PC dimensions and even beyond the borders of vS1 (e.g., L6cc). The gray area denotes 90% of the integral below the respective density curves. (*C*) 1D axon density profiles along the arc (i.e., orthogonal to panel *B*). (*D*) Cell type-specific axon extents along the row and arc revealed asymmetric horizontal spreads, with the exception of L4ss and L5st. (*E*) Quantification of axon projections within (white) and outside (black) the PC reveals cell type- and target layer-specific in/outside PC ratios (from top to bottom: total axon, axon in L1–3, in L4 and L5–6).

IC-unit circuitry (i.e., L5st and L5tt). These columnar pathways were confined to the [supra-]granular stratum and may be regarded as a transition from vertical columnar to horizontal transcolumnar projections, in that septal pathways were organized with respect to, but less confined to columnar dimensions.

Patterned Pathways

Arcish horizontal projections (25% of IC-unit) comprised cell types that displayed transcolumnar axons along the arc and columnar ones along the row (primarily L3py in [supra-]granular, L4sp in supragranular, L5st in granular layers [Fig. 9A]). Strikingly, even though arcish pathways originated from cell types with somata in all layers (also L5tt and L6ct), this horizontal organization principle was primarily found within the [supra-]granular stratum (Fig. 9C). In contrast, rowish axonal projections (13% of IC-unit) were largely confined to infragranular layers. These pathways comprised cell types that were transcolumnar along the row and columnar along the arc (primarily L2py and L6inv (Fig. 9B)).

Unpatterned Pathways

Unpatterned horizontal projections (10% of IC-unit), comprised cell types that were transcolumnar along the row and arc (i.e., primarily L5tt and L6cc). These pathways were found primarily within L5–6, but to a lesser degree also in L4 (Fig. 9C).

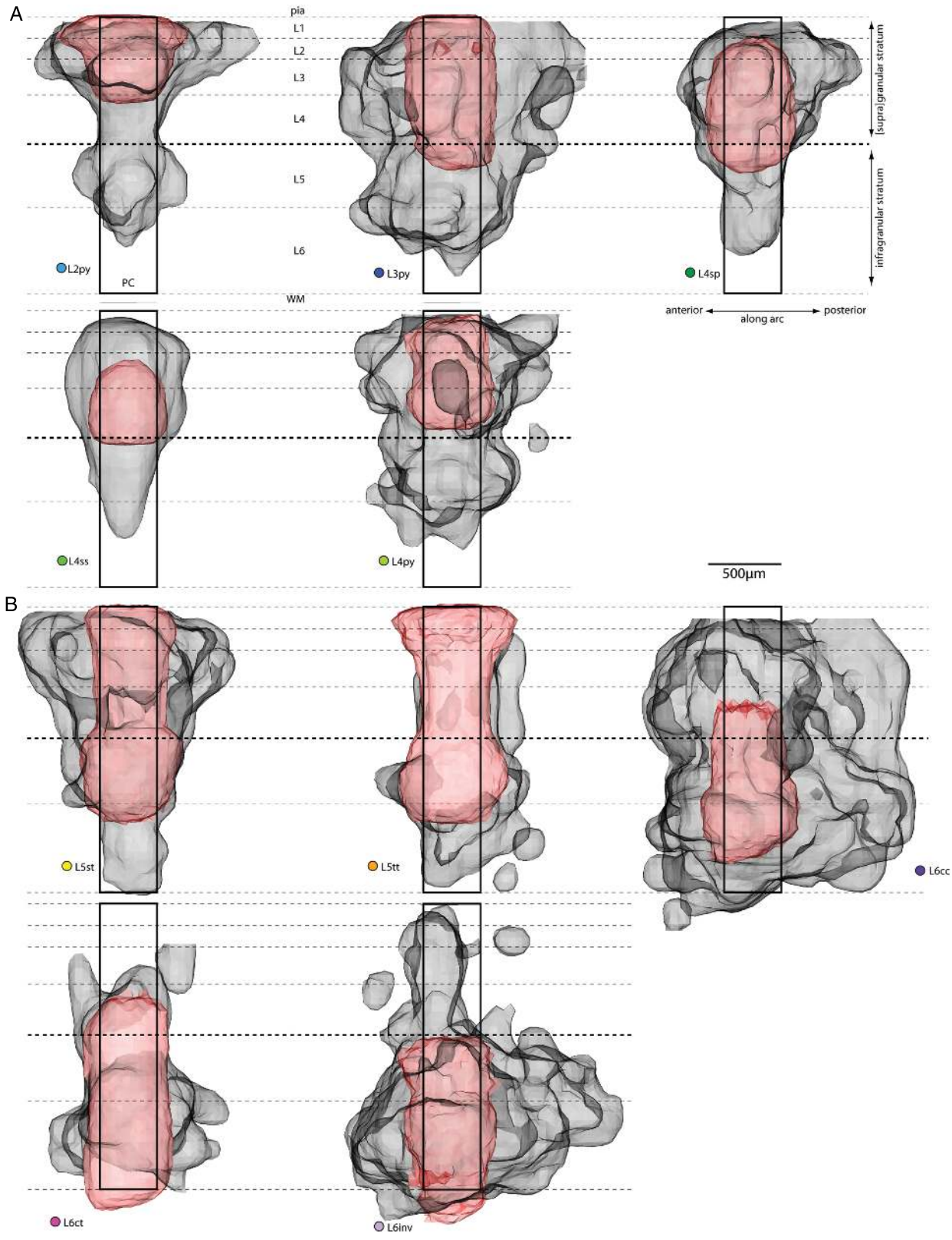

Figure 5. Cell type-specific 3D dendrite and corresponding axon projection volumes. (*A*) Isosurfaces around projection volumes of dendrites (red) and axons (black) of [supra-]granular cell types after extrapolation to the number of excitatory neurons in an average D2 barrel column. Isosurfaces for dendrite and axon projection volumes were calculated at the 99th and 95th percentile, respectively. (*B*) Isosurfaces around projection volumes of dendrites and axons of infragranular cell types (as in panel *A*).

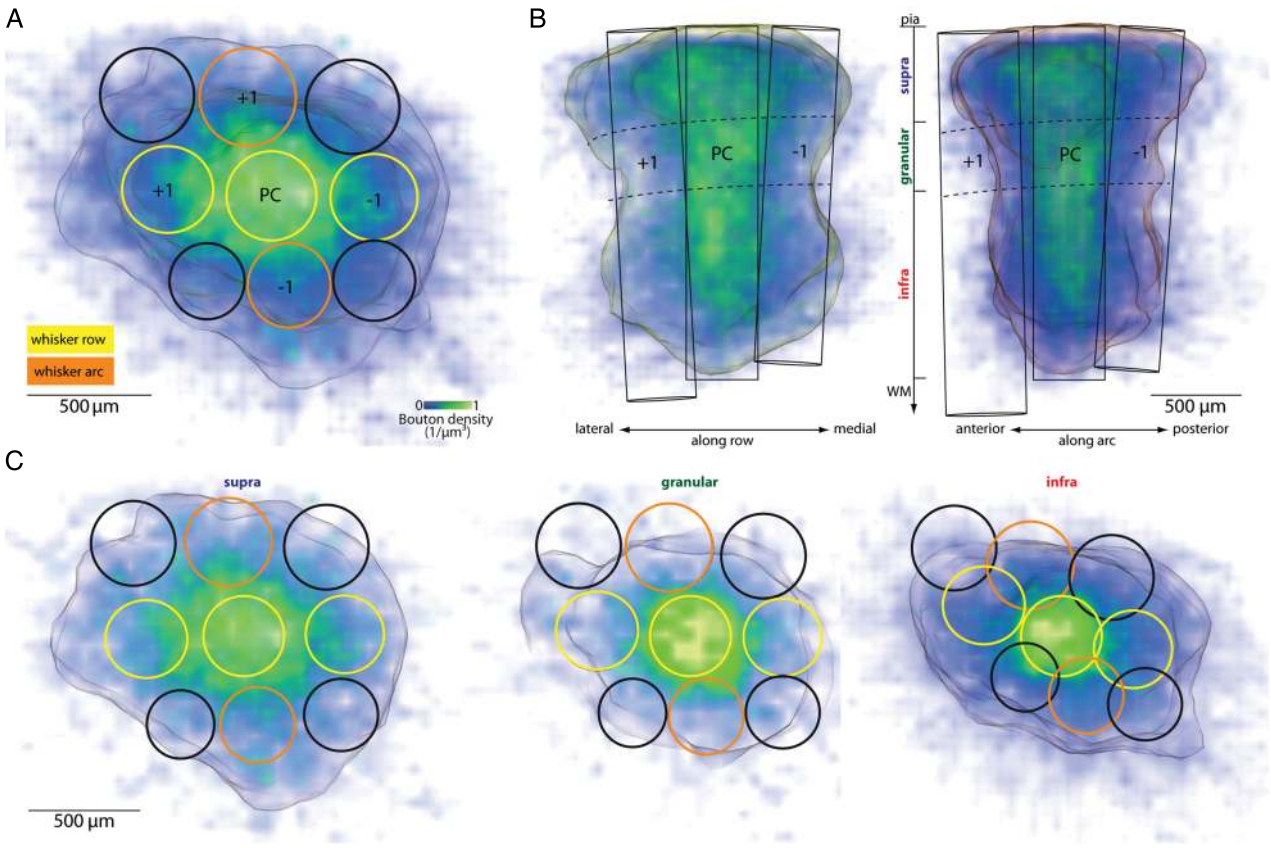

Figure 6. The IC-unit of vS1. (*A*) Top view onto 3D bouton density distribution from axons of all reconstructed excitatory neurons located within a cortical column. The transparent surface area comprised the bouton distribution thresholded at 5% maximal density, revealing that IC axons from a single column activate a volume that comprises ~3 × 3 columns and the septa between them. (*B*) Semi-coronal views of panel A along the row (left) and arc (right) reveal the hourglass shape of the IC-unit. (*C*) Horizontal views of panel A, subdivided in L1–3 (left), L4 (center) and L5–6 (right) reveal target layer-specific asymmetric extents of the IC-unit.

Consequently, unpatterned pathways intermingle with the patterned ones, but primarily with rowish projections in the infragranular stratum (Fig. 9*D*).

Deconstructing the IC-unit into its cell type-, target layer-, and projection pattern-specific contributions thus revealed surprising principles of IC circuit organization. Whereas vertical columnar projections were found throughout the cortical depth, the principles underlying horizontally projecting axons were largely restricted to either the [supra-]granular or infragranular stratum. Specifically, horizontal projections in the [supra-]granular stratum of the IC-unit followed primarily arcish (64%) patterns (septal: 20%, rowish: 9%, unpatterned: 7%). In contrast, the infragranular stratum was structured orthogonally, comprising primarily rowish (53%) patterns (septal: 0%, arcish: 8%, unpatterned: 39%).

Discussion

We provide an unprecedented quantification of the excitatory pathways that interconnect neuronal populations within and across cortical columns in rat vS1. This allowed reconstructing the axonal projection volume originating from a single column, which we refer to as an IC-unit (i.e., in analogy to the lower level TC-unit [Oberlaender et al. 2012]). The cellular resolution of our dataset allowed deconstructing this unit into its cell type-specific components. This yielded 3 major findings. First, the majority of IC axon projects transcolumnar. Second, these horizontal pathways display highly cell type- and target layer-specific projection patterns, which can be grouped into 3 rules: *columnar*, *patterned (arcish/rowish)*, and *unpatterned*. Third, patterned horizontal pathways are exclusive to either [supra-]granular or infragranular layers, subdividing vS1 into 2 orthogonal strata that mirror the organization of the peripheral receptor organs (i.e., whisker arcs and rows).

Sampling of Morphological Cell Types

Our sample comprises all previously reported dendritic cell types of excitatory neurons in rat vS1 (Feldmeyer et al. 2013). Cells in supragranular layers were often grouped as L2/3 neurons, but increasing evidence suggested differentiating between pyramids in L2 and L3 (as reviewed in Petersen and Crochet 2013). In line with this, our data revealed significant differences in axo-dendritic patterns of L2py and L3py, respectively. Cells in L4 were commonly subdivided into L4sp, L4ss, and L4py (Staiger et al. 2004). Our objective classification scheme recovered these 3 cell types. In L5, neurons were grouped as L5st and L5tt (Wise and Jones 1977), which were thought to be located within L5A and L5B (Schubert et al. 2006), respectively. While our classification approach separated between the 2 types, clear assignment to L5A or L5B was not supported by our data. Finally, excitatory cells in L6 were shown to subdivide into 2 general classes, L6ct and L6 cc (Zhang and Deschenes 1997; Kumar and Ohana 2008). Our classification approach clearly separated between these 2 types, but suggested that the group of L6cc contained a subtype (i.e., L6inv) as defined by an (additional) inverted apical dendrite

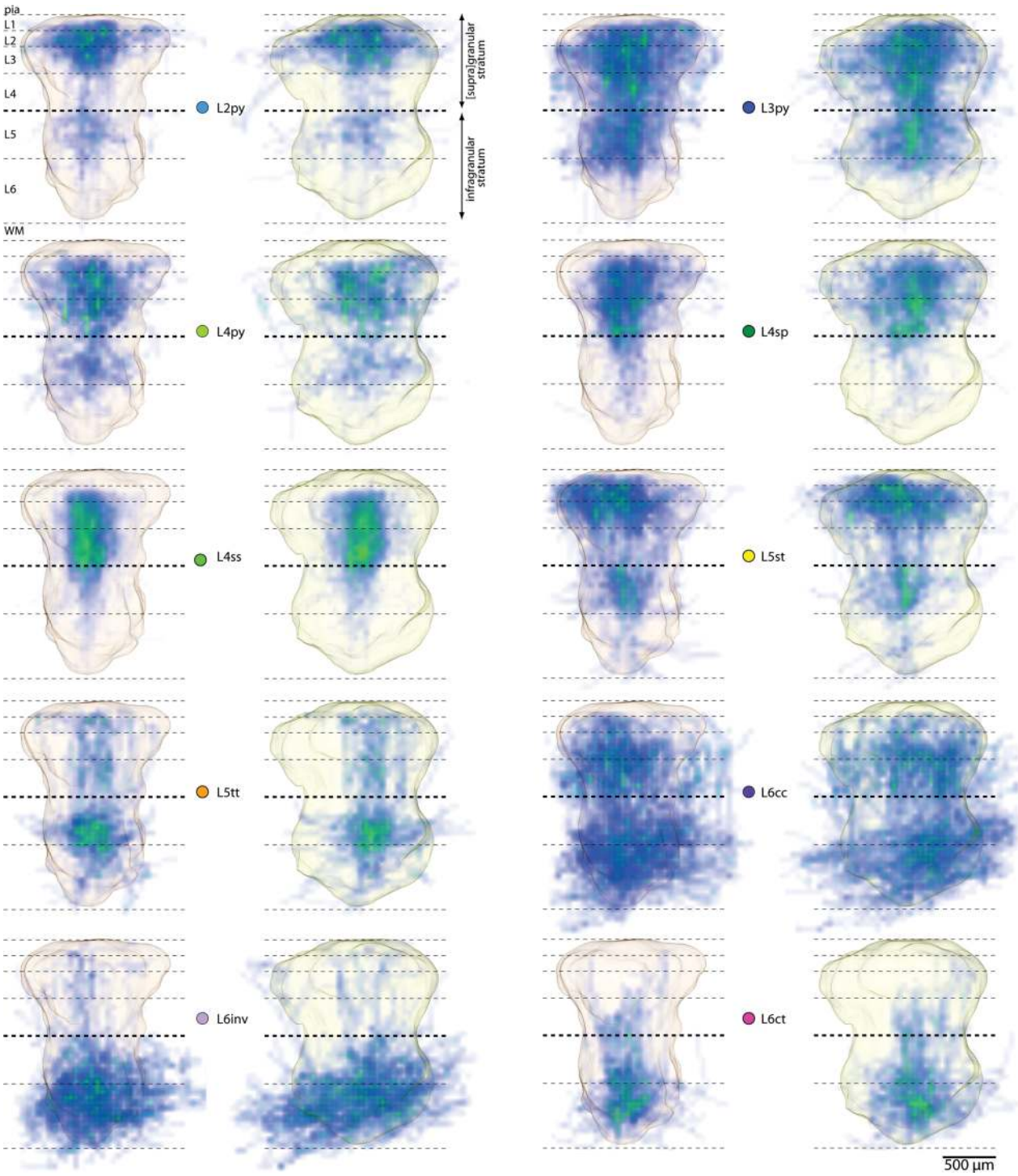

Figure 7. Deconstructing the IC-unit into cell type-specific contributions. Semi-coronal views along the arc (orange) and row (yellow) of all 10 cell type-specific 3D bouton densities within the 3D volume of the IC-unit. Horizontal extents of axonal projection patterns are not only cell type-, but also target layer- and arc/row-specific. For example, axons of L3py define the horizontal extent of the IC-unit in supragranular layers along the arc, but are less elaborate along the row. In contrast, axons of L6inv define the horizontal extent of the IC-unit in infragranular layers along the row, but extend less along the arc.

and axonal projections that were more confined to infragranular layers (see also [Pichon et al. 2012]). Similar dendritic cell types have been reported for other primary cortical areas and species (e.g., cat V1 [Binzegger et al. 2004]). We thus consider our sample of reconstructions as representative for the 10 canonical excitatory cell types of primary sensory cortices.

Definition of an IC-Unit

The lateral dimensions of cortical columns are defined by vertically oriented TC axons (Wimmer et al. 2010), which are the primary relay of sensory-evoked excitation (Brecht and Sakmann 2002b; Constantinople and Bruno 2013). TC-columns are hence regarded as the primary functional units of cortex, because all

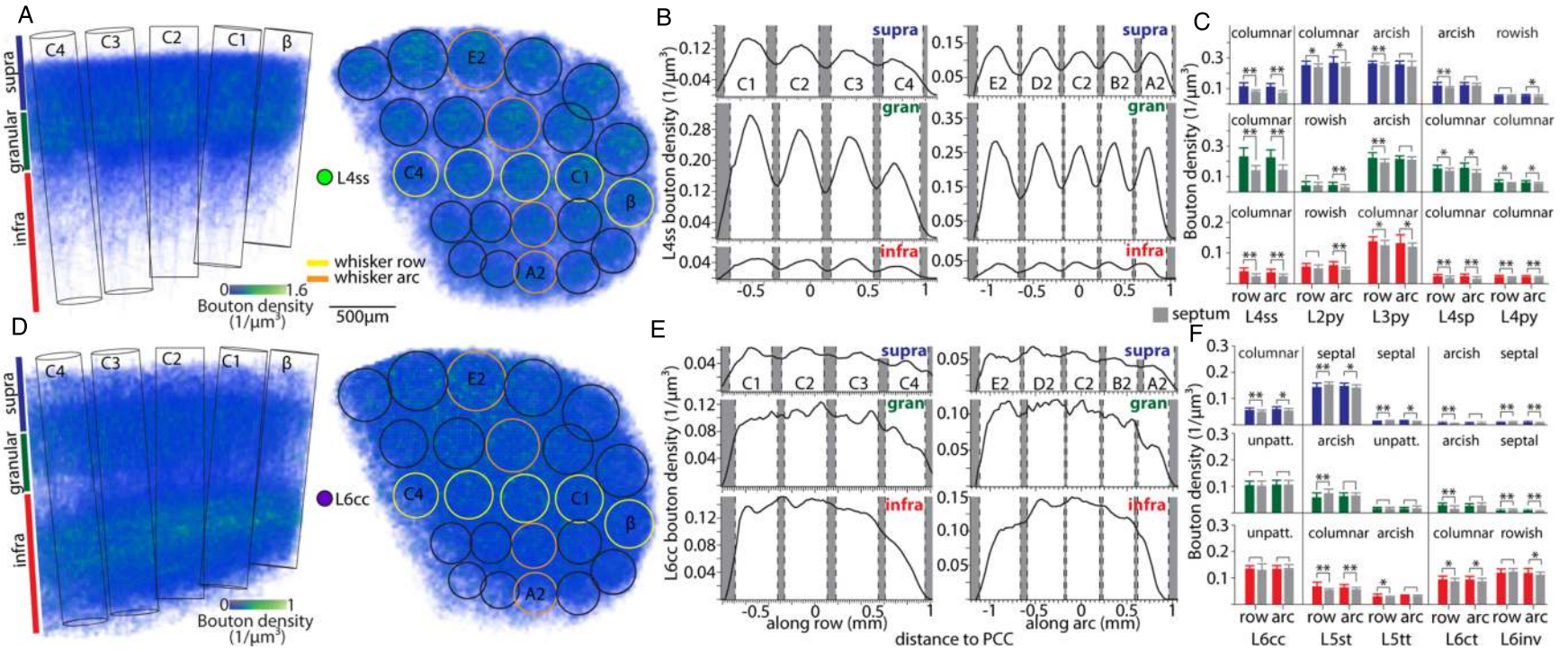

Figure 8. Horizontal axon projections are cell type- and target layer-specific. (*A*) 3D bouton density distribution as derived by integrating and upscaling L4ss axons into a geometrical model of rat vS1. (*B*) Subdividing the bouton density in panel *A* into supragranular, granular, and infragranular distributions allowed calculating target layer-specific 1D horizontal profiles along the row (left) and arc (right), respectively. White and gray areas denote cortical depth- and row/arc-specific extents of columns and septa, respectively. (*C*) Quantification of cell type- and target layer-specific bouton densities in columns and septa along the row and arc, respectively. Stars denote significant differences in bouton density between columns and septa. Significant decreases in bouton density toward septa along the arc and row were termed *columnar* (e.g., L4ss in all layers, left), along the arc but not along the row were termed *rowish* and along the row but not along the arc were termed *arcish*. Significant increases toward septa were termed *septal*. Two asterisks denote cell types whose columnar/septal density differences were more prominent compared with those with one asterisk (see Materials and Methods). (*D*) 3D bouton density distribution of L6cc axons in vS1. (*E*) Target layer-specific 1D horizontal profiles along the row (left) and arc of L6cc (right), respectively. (*F*) Assignment to columnar, rowish, arcish, and septal axon projection patterns as in panel *C*. Density profiles that did not differ between columns and septa, neither along the row nor the arc, were termed *unpatterned* (e.g., L6cc neurons in granular layers).

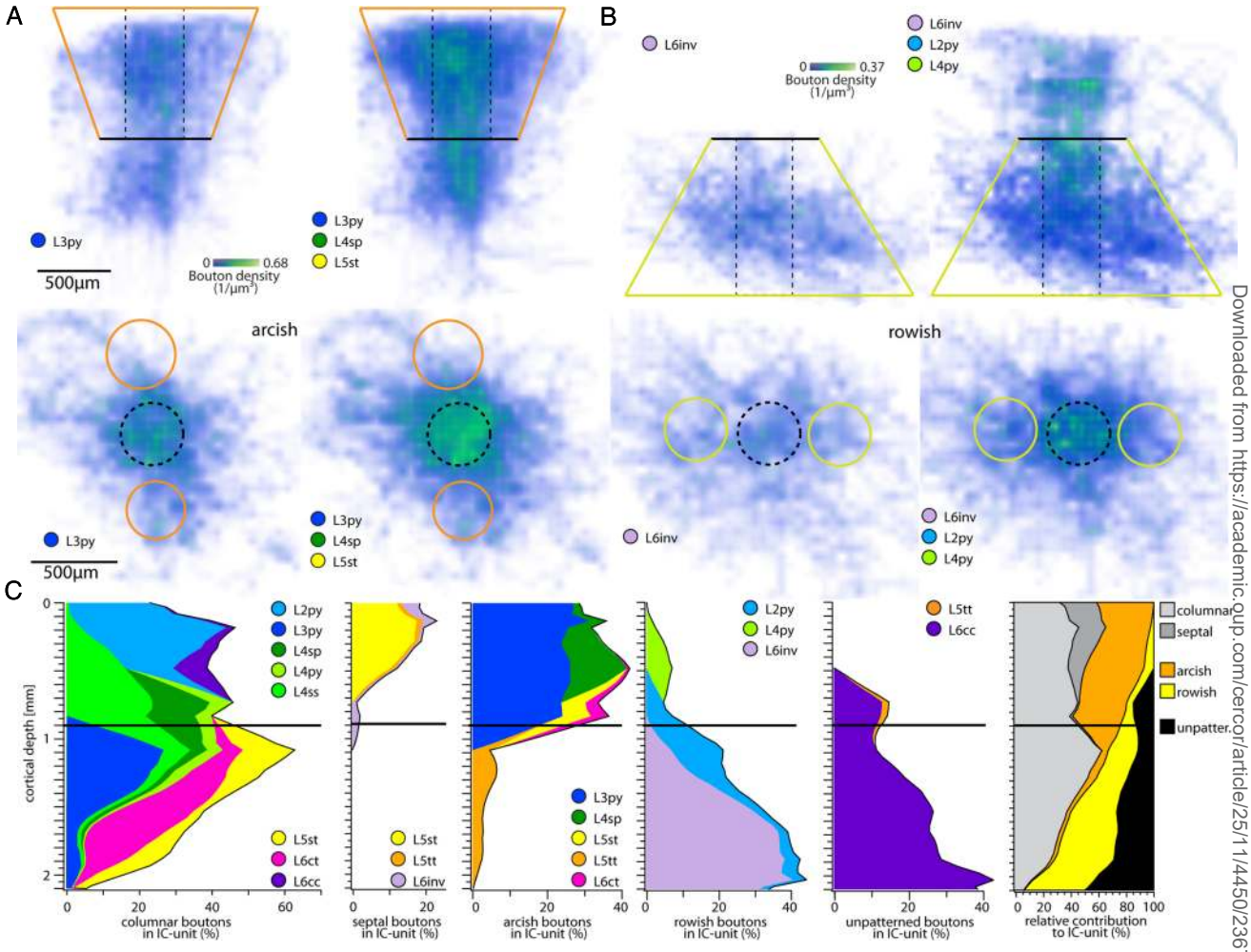

Figure 9. Deconstructing the IC-unit reveals 2 orthogonal horizontal strata. (*A*) Semi-coronal (top) and top views (bottom) of bouton densities along the arc of the major (L3py, left) and all cell types (right) that contribute to arcish pathways reveal that such horizontal patterns are largely restricted to the [supra-]granular stratum. (*B*) Bouton densities along the row of the major (L6inv, left) and all cell types (right) that contribute to rowish pathways reveal that such horizontal patterns are largely restricted to the infragranular stratum. (*C*) Quantification of the relative cell type-specific contributions to columnar/septal, patterned (rowish/arcish) and unpatterned pathways and to the total number of boutons within the IC-unit. Columnar pathways were present throughout the cortical depth, reaching a maximum within upper L5 (i.e., ~60% of all boutons at this depth arose from axons assigned to the columnar projection pattern). Septal pathways were largely confined to supragranular layers. Patterned pathways segregate vS1 into 2 orthogonal strata, arcish, and rowish, in the [supra-]granular and infragranular stratum, respectively. Unpatterned projections contribute primarily to the infragranular stratum, and to a lesser degree to granular L4. (*D*) Boutons from axons assigned to the 5 organizational principles intermingle with each other across the entire cortical depth. Columnar pathways represent ~45% of the IC-unit circuitry across all layers. In contrast, the transcolumnar horizontal pathways are largely specific for the respective [supra-]granular (septal and arcish) and infragranular (rowish and unpatterned) stratum.

neurons in the respective volumes receive similarly tuned monosynaptic TC input (Brecht and Sakmann 2002a; Brecht et al. 2003; Manns et al. 2004). In line with this, we define the volume innervated by horizontal axonal projections from neurons with somata in a TC-column as the IC-unit. Because all neurons in this volume can receive monosynaptic IC input from neurons located in the TC-column, we regard the IC-unit as the first higher-order functional entity of sensory cortex. Deconstructing the IC-unit of vS1 into its cell type-specific components demonstrated that the horizontal axonal projections that give rise to its hourglass shape are not uniformly structured. Instead, cell type- and target layer-specific projection patterns subdivided vS1 into 2 horizontal strata, with axons in the [supra-]granular and infragranular stratum following arcish (and septal) and rowish (and unpatterned) principles, respectively.

Functional Implications of the IC-Unit

Columnar Pathways

The majority of vertically oriented axons (i.e., largely confined to the lateral dimensions of the TC-column) remained local within the layer containing the respective somata. However, 2 cell types displayed columnar axons that projected translaminar: L4ss→L2/3 and L3py→L5. Because TC axons are most dense in L4, where they define the lateral extent of a barrel column, the L4ss→L3py→L5 pathway can be regarded as an extension of the columnar TC→L4 pathway, which has been previously referred to as a canonical microcircuit of sensory cortices (Gilbert and Wiesel 1979; Douglas and Martin 2004). Our data support this hypothesis. However, we show that this circuit represents only a minor fraction of the IC circuitry (i.e., axon/bouton distribution),

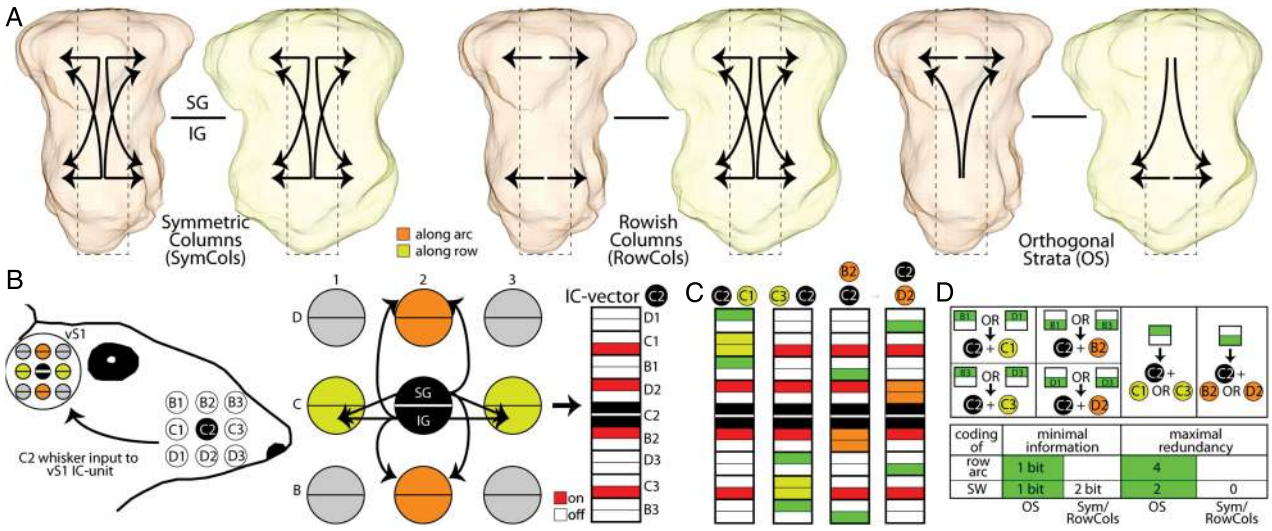

Figure 10. Models of transcolumnar whisker-evoked signal flow. (*A*) Simplification of the IC-unit into 9 columns, each consisting of one [supra-]granular and one infragranular compartment, respectively. The compartments were interconnected based on 3 different transcolumnar principles. (Left) The *SymCols* model assumes no specificity of transcolumnar pathways. (Center) The *RowCols* model assumes that transcolumnar pathways are in general rowish. (Right) The *OS* model is based on the anatomical findings in the present study. (*B*) Investigation of principal whisker-evoked (C2, black) signal flow within the OS model of the IC-unit, as quantified by an 18-dimensional (i.e., 18 compartments) binary IC-vector (on = 1 [red]: signal spread into the respective compartment; off = 0 [white]: no spread). (*C*) Quantification of the respective IC-vectors for 4 different combinations of 2-whisker inputs. (*D*) In the OS model, active compartments in [supra-]granular or infragranular strata of nonstimulated columns can unambiguously (green) encode the identity of the additional stimulated whisker. Furthermore, activation of a single [supra-]granular or infragranular compartment (1 bit) in any of the 4 nonstimulated (diagonal) columns (redundancy: 4) is sufficient for an ideal observer to decode whether 2 whiskers in the same row or arc provided the input, respectively. The identity of the surround whisker can be encoded similarly (i.e., by nonstimulated columns) in the other models, but requires twice the information (i.e., 2 bits, redundancy of 0). In contrast, for an ideal observer that just monitors activity in the nonstimulated columns, decoding whether the second stimulated whisker was in the same row or arc as the principal whisker, is impossible in the Sym/RowCols models.

which is otherwise structured by additional highly specific transcolumnar horizontal pathways.

Unpatterned Pathways

These pathways originated primarily from L6cc, whose axons innervate all columns/septa surrounding the PC. Because we previously showed that L6cc display reliable and short-latency whisker-evoked spiking responses (Oberlaender et al. 2012), we hypothesize that unpatterned pathways give rise to the fast horizontal spread of single whisker-evoked excitation (Petersen et al. 2003), influencing (e.g., broadening) TC-evoked receptive fields (RFs) of infragranular neurons. In line with this hypothesis, recent findings in mouse V1 revealed that L6cc encompass a broad spectrum of selectivity to stimulus orientation and are predominantly innervated by deep layer neurons (Velez-Fort et al. 2014), suggesting that broadening of TC RFs by unpatterned L6cc projections may be generalizable to other sensory systems and species.

Patterned Pathways

It was suggested that during exploratory whisking (i.e., back and forth movement of the whiskers) coding of spatial (e.g., object shape) and temporal (e.g., object movement) sensory information may be achieved by integrating inputs from multiple whiskers of the same arc and row, respectively (Celikel and Sakmann 2007). Providing an anatomical framework for this hypothesis, we found that the majority of horizontal IC projections in the [supra-]granular and infragranular stratum interconnected columns that represent whiskers of the same arc and row, respectively. Thus, our data suggest that vS1 segregates and differentiates between rowish and arcish multi whisker inputs.

To investigate potential functional implications of arcish/rowish input segregation during transcolumnar communication via 2 orthogonal strata, we generated a flow model by simplifying the IC-unit to 9 columns (PC and the 8 adjacent SCs), each comprising one [supra-]granular and one infragranular compartment. The resulting 18 compartments of the vS1 model were then interconnected according to 3 different transcolumnar rules (Fig. 10A). First, a *Symmetric Columns* (SymCols) model, as suggested by studies of the Blue Brain Project (Markram 2006), assumes no specificity of horizontally projecting axons. The resulting transcolumnar pathways hence connect the compartments of the PC with the respective ones of the SCs symmetrically along the arc and row. Second, a *Rowish Columns* (RowCols) model, as suggested by bulk injections into vS1 (Bernardo et al. 1990), assumes that horizontally projecting axons are in general organized by the rowish pattern. Finally, an *Orthogonal Strata* (OS) model interconnects the 2 compartments of each column based on the observations in the present study.

Using these models, we explored how whisker-evoked excitation may spread within the differently interconnected IC-units of vS1. Figure 10*B* illustrates the spread of feed-forward excitation in the OS model for input from the C2 (principal) whisker. The spread of excitation was quantified by converting all compartments of the model into an 18 dimensional *IC-vector*. Each entry (bit) of the vector was binary, being either 1 or 0, depending on whether excitation spread into the respective compartment or not.

Single whisker inputs do not show major differences between the 3 models. In contrast, multi whisker inputs demonstrate advantages for stimulus discrimination by an independent observer (i.e., receives signals with equal strength from both strata) if transcolumnar communication is organized via OS. Figure 10C illustrates the signal spreads in the OS model for 4 different combinations of 2-whisker inputs. Multiple bits of the respective IC-vectors were exclusively active (green) for one specific 2-whisker combination. For example, activity in the [supra-]granular

compartment of B1 and D1 can only arise if the C1 whisker provided additional input to C2. Thus, from the activity in the [supra-]granular compartments of the nonstimulated B1 or D1 columns (i.e., 1 bit, redundancy of 2), an independent observer could unambiguously decode that the stimulated surround whisker was C1 (Fig. 10*D*). Moreover, a single active [supra-]granular or infragranular compartment in any of the 4 nonstimulated columns is sufficient to encode whether the second stimulated whisker was in the same row or arc as the principal whisker (i.e., 1 bit, redundancy of 4).

The identity of the surround whisker can be encoded similarly in the other models, but requires twice the information (i.e., 2 bits, redundancy of 0). In contrast, for an ideal observer that just monitors activity in the nonstimulated columns, decoding whether the second stimulated whisker was in the same row or arc as the principal whisker, is impossible in the Sym/RowCols models. Consequently, organization of transcolumnar communication via orthogonal strata could be more effective and more robust for coding 2-whisker inputs compared with any one of the previously suggested models of transcolumnar communication. Furthermore, orthogonal strata of horizontally projecting axons could provide anticipatory information to columns (e.g., about object shape and/or whisker contact), whose respective whiskers have not yet touched the object.

Conclusion

In the present study, we quantified all excitatory pathways in rat vS1 and found multiple highly specialized principles of transcolumnar axonal projections. Thus, general functional phenomena of primary sensory cortices, such as broadening of neuronal RFs between thalamus and cortex (Kwegyir-Afful et al. 2005), tuning of individual synapses to multiple stimuli (as observed in vS1 (Varga et al. 2011), V1 (Jia et al. 2010), and A1 (Grienberger et al. 2012)) and ultimately understanding of complex responses to natural stimuli (Ramirez et al. 2014), will remain elusive without quantification of the pathways by which cortical columns communicate. Consequently, we argue that the concept of cortical columns (TC-units) as the minimal entity of cortical processing has to be extended at the next level of structural representation to IC-units, whose organizational principles may in part be similar (e.g., canonical circuit, unpatterned projections in L6), but in general specific for each sensory system (e.g., patches between orientation columns in V1, arcish/rowish strata in vS1). Thus, the state-of-the-art of describing cortical circuits by intracolumnar (vertical) pathways has to be complemented with quantification of transcolumnar (horizontal) projection patterns, and we consider our approach of generating/deconstructing IC-units as a generalizable roadmap to provide such complete 3D circuit diagrams for other sensory systems and species.

Supplementary Material

Supplementary material can be found at: http://www.cercor.oxfordjournals.org.

Authors' Contributions

M.O., B.S., and C.D.K. conceived and designed the project. R.N., B.S., H.M., and C.D.K. designed and performed in vivo experiments. R.N. and M.O. performed anatomical reconstructions. R.E., A.J., and M.O. developed analysis routines. M.O. performed data analysis and wrote the manuscript with feedback from all authors.

Funding

Funding was provided by the Max Planck Florida Institute (A.J., M.O., B.S.), the Studienstiftung des deutschen Volkes (R.E.), the Bernstein Center for Computational Neuroscience, funded by German Federal Ministry of Education and Research Grant BMBF/FKZ 01GQ1002 (R.E., R.N., M.O.), the Max Planck Institute for Biological Cybernetics (R.E., R.N., M.O.), the Werner Reichardt Center for Integrative Neuroscience (M.O.), and by the VU University, Amsterdam (C.D.K., H.M., R.N.). Funding to pay the Open Access publication charges for this article was provided by the Max Planck Florida Institute for Neuroscience.

Notes

We thank the Anatomy Institute of the University of Tuebingen for their generous support, Randy M. Bruno and Zimbo S.R.M. Boudewijns for providing some of the in vivo-labeled neurons, Brendan Lodder and Anton Pieneman for technical assistance, Hyun Jae Jang for discussions of the flow model and Lothar Baltruschat, Tatjana Kleele and Kevin Pels for proof-editing neuron reconstructions. *Conflict of Interest*: None declared.

References

Ankerst M, Breunig M, Kriegel HP, Sander J. 1999. OPTICS: Ordering Points To Identify the Clustering Structure. ACM SIGMOD'99 Int Conf on Management of Data, 49–60.

Bernardo KL, McCasland JS, Woolsey TA, Strominger RN. 1990. Local intra- and interlaminar connections in mouse barrel cortex. J Comp Neurol. 291:231–255.

Binzegger T, Douglas RJ, Martin KA. 2004. A quantitative map of the circuit of cat primary visual cortex. J Neurosci. 24:8441–8453.

Bosking WH, Zhang Y, Schofield B, Fitzpatrick D. 1997. Orientation selectivity and the arrangement of horizontal connections in tree shrew striate cortex. J Neurosci. 17:2112–2127.

Braitenberg V. 1962. A note on myeloarchitectonics. J Comp Neurol. 118:141–156.

Brecht M, Roth A, Sakmann B. 2003. Dynamic receptive fields of reconstructed pyramidal cells in layers 3 and 2 of rat somatosensory barrel cortex. J Physiol. 553:243–265.

Brecht M, Sakmann B. 2002a. Dynamic representation of whisker deflection by synaptic potentials in spiny stellate and pyramidal cells in the barrels and septa of layer 4 rat somatosensory cortex. J Physiol. 543:49–70.

Brecht M, Sakmann B. 2002b. Whisker maps of neuronal subclasses of the rat ventral posterior medial thalamus, identified by whole-cell voltage recording and morphological reconstruction. J Physiol. 538:495–515.

Bruno RM, Hahn TT, Wallace DJ, de Kock CP, Sakmann B. 2009. Sensory experience alters specific branches of individual corticocortical axons during development. J Neurosci. 29:3172–3181.

Brown SP, Hestrin S. 2009. Intracortical circuits of pyramidal neurons reflect their long-range axonal targets. Nature. 457:1133–1136.

Celikel T, Sakmann B. 2007. Sensory integration across space and in time for decision making in the somatosensory system of rodents. Proc Natl Acad Sci USA. 104:1395–1400.

Constantinople CM, Bruno RM. 2013. Deep cortical layers are activated directly by thalamus. Science. 340:1591–1594.

Creutzfeldt OD, Garey LJ, Kuroda R, Wolff JR. 1977. The distribution of degenerating axons after small lesions in the intact and isolated visual cortex of the cat. Exp Brain Res. 27:419–440.

de Kock CP, Bruno RM, Spors H, Sakmann B. 2007. Layer- and cell-type-specific suprathreshold stimulus representation in rat primary somatosensory cortex. J Physiol. 581:139–154.

Dercksen VJ, Hege HC, Oberlaender M. 2014. The Filament Editor: an interactive software environment for visualization, proof-editing and analysis of 3D neuron morphology. Neuroinformatics. 12:325–339.

Douglas RJ, Martin KA. 2004. Neuronal circuits of the neocortex. Annu Rev Neurosci. 27:419–451.

Egger R, Dercksen VJ, Udvary D, Hege HC, Oberlaender M. 2014. Generation of dense statistical connectomes from sparse morphological data. Front Neuroanat. 8:129.

Egger R, Narayanan RT, Helmstaedter M, de Kock CP, Oberlaender M. 2012. 3D reconstruction and standardization of the rat vibrissal cortex for precise registration of single neuron morphology. PLoS Comput Biol. 8:e1002837.

Egger V, Nevian T, Bruno RM. 2008. Subcolumnar dendritic and axonal organization of spiny stellate and star pyramid neurons within a barrel in rat somatosensory cortex. Cereb Cortex. 18:876–889.

Ego-Stengel V, Mello e Souza T, Jacob V, Shulz DE. 2005. Spatiotemporal characteristics of neuronal sensory integration in the barrel cortex of the rat. J Neurophysiol. 93:1450–1467.

Feldmeyer D, Brecht M, Helmchen F, Petersen CC, Poulet JF, Staiger JF, Luhmann HJ, Schwarz C. 2013. Barrel cortex function. Prog Neurobiol. 103:3–27.

Feldmeyer D, Egger V, Lubke J, Sakmann B. 1999. Reliable synaptic connections between pairs of excitatory layer 4 neurones within a single 'barrel' of developing rat somatosensory cortex. J Physiol. 521(Pt 1):169–190.

Feldmeyer D, Lubke J, Sakmann B. 2006. Efficacy and connectivity of intracolumnar pairs of layer 2/3 pyramidal cells in the barrel cortex of juvenile rats. J Physiol. 575:583–602.

Fisken RA, Garey LJ, Powell TP. 1975. The intrinsic, association and commissural connections of area 17 on the visual cortex. Philos Trans R Soc Lond Ser B, Biol Sci. 272:487–536.

Gilbert CD, Wiesel TN. 1983. Clustered intrinsic connections in cat visual cortex. J Neurosci. 3:1116–1133.

Gilbert CD, Wiesel TN. 1979. Morphology and intracortical projections of functionally characterised neurones in the cat visual cortex. Nature. 280:120–125.

Goldman-Rakic PS. 1995. Cellular basis of working memory. Neuron. 14:477–485.

Grienberger C, Adelsberger H, Stroh A, Milos RI, Garaschuk O, Schierloh A, Nelken I, Konnerth A. 2012. Sound-evoked network calcium transients in mouse auditory cortex in vivo. J Physiol. 590:899–918.

Horikawa K, Armstrong WE. 1988. A versatile means of intracellular labeling: injection of biocytin and its detection with avidin conjugates. J Neurosci Methods. 25:1–11.

Hubel DH, Wiesel TN. 1959. Receptive fields of single neurones in the cat's striate cortex. J Physiol. 148:574–591.

Huntley GW, Jones EG. 1991. Relationship of intrinsic connections to forelimb movement representations in monkey motor cortex: a correlative anatomic and physiological study. J Neurophysiol. 66:390–413.

Jia H, Rochefort NL, Chen X, Konnerth A. 2010. Dendritic organization of sensory input to cortical neurons in vivo. Nature. 464:1307–1312.

Keller A. 1993. Intrinsic synaptic organization of the motor cortex. Cereb Cortex. 3:430–441.

Keller A, Asanuma H. 1993. Synaptic relationships involving local axon collaterals of pyramidal neurons in the cat motor cortex. J Comp Neurol. 336:229–242.

Kumar P, Ohana O. 2008. Inter- and intralaminar subcircuits of excitatory and inhibitory neurons in layer 6a of the rat barrel cortex. J Neurophysiol. 100:1909–1922.

Kwegyir-Afful EE, Bruno RM, Simons DJ, Keller A. 2005. The role of thalamic inputs in surround receptive fields of barrel neurons. J Neurosci. 25:5926–5934.

Lefort S, Tomm C, Floyd Sarria JC, Petersen CC. 2009. The excitatory neuronal network of the C2 barrel column in mouse primary somatosensory cortex. Neuron. 61:301–316.

Levitt JB, Lewis DA, Yoshioka T, Lund JS. 1993. Topography of pyramidal neuron intrinsic connections in macaque monkey prefrontal cortex (areas 9 and 46). J Comp Neurol. 338:360–376.

Lubke J, Egger V, Sakmann B, Feldmeyer D. 2000. Columnar organization of dendrites and axons of single and synaptically coupled excitatory spiny neurons in layer 4 of the rat barrel cortex.J Neurosci. 20:5300–5311.

Manns ID, Sakmann B, Brecht M. 2004. Sub- and suprathreshold receptive field properties of pyramidal neurones in layers 5A and 5B of rat somatosensory barrel cortex.J Physiol. 556:601–622.

Markram H. 2006. The blue brain project. Nat Rev Neurosci. 7:153–160.

Meyer HS, Egger R, Guest JM, Foerster R, Reissl S, Oberlaender M. 2013. Cellular organization of cortical barrel columns is whisker-specific. Proc Natl Acad Sci USA. 110:19113–19118.

Meyer HS, Wimmer VC, Oberlaender M, de Kock CP, Sakmann B, Helmstaedter M. 2010. Number and laminar distribution of neurons in a thalamocortical projection column of rat vibrissal cortex. Cereb Cortex. 20:2277–2286.

Mountcastle VB. 1957. Modality and topographic properties of single neurons of cat's somatic sensory cortex. J Neurophysiol. 20:408–434.

Narayanan RT, Mohan H, Broersen R, de Haan R, Pieneman AW, de Kock CP. 2014. Juxtasomal biocytin labeling to study the structure–function relationship of individual cortical neurons. J Visualized Exp. (8):e51359.

Nauta WJ, Gygax PA. 1954. Silver impregnation of degenerating axons in the central nervous system: a modified technic. Stain Technol. 29:91–93.

Nikolenko V, Poskanzer KE, Yuste R. 2007. Two-photon photostimulation and imaging of neural circuits. Nat Methods. 4:943–950.

Oberlaender M, Boudewijns ZS, Kleele T, Mansvelder HD, Sakmann B, de Kock CP. 2011. Three-dimensional axon morphologies of individual layer 5 neurons indicate cell type-specific intracortical pathways for whisker motion and touch. Proc Natl Acad Sci USA. 108:4188–4193.

Oberlaender M, Bruno RM, Sakmann B, Broser PJ. 2007. Transmitted light brightfield mosaic microscopy for three-dimensional tracing of single neuron morphology. J Biomed Optics. 12:064029.

Oberlaender M, de Kock CP, Bruno RM, Ramirez A, Meyer HS, Dercksen VJ, Helmstaedter M, Sakmann B. 2012. Cell type-specific three-dimensional structure of thalamocortical circuits in a column of rat vibrissal cortex. Cereb Cortex. 22:2375–2391.

Petersen CC, Crochet S. 2013. Synaptic computation and sensory processing in neocortical layer 2/3. Neuron. 78:28–48.

Petersen CC, Grinvald A, Sakmann B. 2003. Spatiotemporal dynamics of sensory responses in layer 2/3 of rat barrel cortex measured in vivo by voltage-sensitive dye imaging combined with whole-cell voltage recordings and neuron reconstructions. J Neurosci. 23:1298–1309.

Petreanu L, Mao T, Sternson SM, Svoboda K. 2009. The subcellular organization of neocortical excitatory connections. Nature. 457:1142–1145.

Pichon F, Nikonenko I, Kraftsik R, Welker E. 2012. Intracortical connectivity of layer VI pyramidal neurons in the somatosensory cortex of normal and barrelless mice. Eur J Neurosci. 35:855–869.

Pinault D. 1996. A novel single-cell staining procedure performed in vivo under electrophysiological control: morpho-functional features of juxtacellularly labeled thalamic cells and other central neurons with biocytin or Neurobiotin. J Neurosci Methods. 65:113–136.

Rainer G, Asaad WF, Miller EK. 1998. Memory fields of neurons in the primate prefrontal cortex. Proc Natl Acad Sci USA. 95:15008–15013.

Ramirez A, Pnevmatikakis EA, Merel J, Paninski L, Miller KD, Bruno RM. 2014. Spatiotemporal receptive fields of barrel cortex revealed by reverse correlation of synaptic input. Nat Neurosci. 17:866–875.

Rockland KS, Lund JS. 1982. Widespread periodic intrinsic connections in the tree shrew visual cortex. Science. 215: 1532–1534.

Rockland KS, Lund JS, Humphrey AL. 1982. Anatomical binding of intrinsic connections in striate cortex of tree shrews (Tupaia glis). J Comp Neurol. 209:41–58.

Schubert D, Kotter R, Luhmann HJ, Staiger JF. 2006. Morphology, electrophysiology and functional input connectivity of pyramidal neurons characterizes a genuine layer va in the primary somatosensory cortex. Cereb Cortex. 16:223–236.

Staiger JF, Flagmeyer I, Schubert D, Zilles K, Kotter R, Luhmann HJ. 2004. Functional diversity of layer IV spiny neurons in rat somatosensory cortex: quantitative morphology of electrophysiologically characterized and biocytin labeled cells. Cereb Cortex. 14:690–701.

Svoboda K. 2011. The past, present, and future of single neuron reconstruction. Neuroinformatics. 9:97–98.

Varga Z, Jia H, Sakmann B, Konnerth A. 2011. Dendritic coding of multiple sensory inputs in single cortical neurons in vivo. Proc Natl Acad Sci USA. 108:15420–15425.

Velez-Fort M, Rousseau CV, Niedworok CJ, Wickersham IR, Rancz EA, Brown AP, Strom M, Margrie TW. 2014. The stimulus selectivity and connectivity of layer six principal cells reveals cortical microcircuits underlying visual processing. Neuron. 83:1431–1443.

Weiss DS, Keller A. 1994. Specific patterns of intrinsic connections between representation zones in the rat motor cortex. Cereb Cortex. 4:205–214.

Wimmer VC, Bruno RM, de Kock CP, Kuner T, Sakmann B. 2010. Dimensions of a projection column and architecture of VPM and POm axons in rat vibrissal cortex. Cereb Cortex. 20:2265–2276.

Wise SP, Jones EG. 1977. Cells of origin and terminal distribution of descending projections of the rat somatic sensory cortex. J Comp Neurol. 175:129–157.

Wong-Riley M. 1979. Changes in the visual system of monocularly sutured or enucleated cats demonstrable with cytochrome oxidase histochemistry. Brain Res. 171: 11–28.

Woolsey TA, Van der Loos H. 1970. The structural organization of layer IV in the somatosensory region (SI) of mouse cerebral cortex. The description of a cortical field composed of discrete cytoarchitectonic units. Brain Res. 17:205–242.

Zhang ZW, Deschenes M. 1997. Intracortical axonal projections of lamina VI cells of the primary somatosensory cortex in the rat: a single-cell labeling study. J Neurosci. 17:6365–6379.